CONFINEMENT AND TRANSPORT RESEARCH IN ALCATOR C-MOD

M. GREENWALD,[a]* N. BASSE,[a] P. BONOLI,[a] R. BRAVENEC,[b] E. EDLUND,[a] D. ERNST,[a] C. FIORE,[a] R. GRANETZ,[a] A. HUBBARD,[a] J. HUGHES,[a] I. HUTCHINSON,[a] J. IRBY,[a] B. LaBOMBARD,[a] L. LIN,[a] Y. LIN,[a] B. LIPSCHULTZ,[a] E. MARMAR,[a] D. MIKKELSEN,[c] D. MOSSESSIAN,[a] P. PHILLIPS,[b] M. PORKOLAB,[a] J. RICE,[a] W. ROWAN,[b] S. SCOTT,[c] J. SNIPES,[a] J. TERRY,[a] S. WOLFE,[a] S. WUKITCH,[a] and K. ZHUROVICH[a]

[a]*Massachusetts Institute of Technology, Plasma Science and Fusion Center, Cambridge, Massachusetts 02138*
[b]*University of Texas, Austin, Texas*
[c]*Princeton Plasma Physics Laboratory, Princeton, New Jersey*

Received November 22, 2005
Accepted for Publication February 2, 2006

Global and local transport experiments in ohmic, L-mode and H-mode regimes on the Alcator C-Mod tokamak are summarized. For ohmic plasmas, earlier results derived for energy confinement scaling in the Alcator (linear) regime have been confirmed, and the saturated confinement regime has been shown to be equivalent to that of L-mode. For auxiliary heated regimes, C-Mod provided a unique laboratory to test the standard scaling laws that had been previously derived. C-Mod's L-mode performance matches the L-mode scaling laws quite well, but the confinement times in H-mode were about 50% above the existing H-mode scaling laws. This difference was significant and pointed up shortcomings in the range and conditioning of the existing database. H-mode studies emphasize quasi-steady regimes with good energy confinement, no impurity accumulation, and no large edge-localized modes. A new H-mode regime, where the pedestal is regulated by a continuous quasi-coherent mode, has been investigated extensively. The regime is most accessible at higher safety factor, triangularity, and collisionality and at low ion mass, suggesting that the mode is a form of resistive ballooning. Studies on C-Mod first showed the quantitative link between edge temperatures, core temperature gradients, and core confinement. This link unified L-mode and H-mode and established a strong connection between local and global transport. Further work on the role of critical gradient lengths and marginal stability lent quantitative support to the ion temperature gradient theories for ion transport and have helped elucidate nonlinear saturation mechanisms for the turbulence. Local transport studies demonstrated connections between transport channels, with energy, particle, and momentum transport varying across regimes in similar ways. Experiments carried out in collaboration with the DIII-D, ASDEX-U, and JET groups confirmed the dimensionless scaling approach over the widest available range in machine sizes. These studies suggest that plasma physics is the dominant influence on transport in the core and pedestal for standard L- and H-mode discharges. Dimensionless scaling experiments have shown a strong improvement in confinement with the normalized gyro size ($1/\rho^*$). Confinement was found to be Bohm-like in L-mode and gyro-Bohm-like in H-mode. These experiments also showed a strong degradation in confinement with collisionality.

KEYWORDS: *magnetic confinement, Alcator C-Mod, tokamak*

NOTE: Some figures in this paper are in color only in the electronic version.

I. INTRODUCTION

Alcator C-Mod is a compact high-field diverted tokamak with molybdenum plasma-facing components and strong ion cyclotron resonance frequency (ICRF) heating. It has a nominal major radius $R = 0.66$ m and minor radius $a = 0.22$ m. For transport studies, parameter range spans are $I_P = 0.24$ to 2 MA, $B_T = 2.0$ to 8.0 T, $P_{INPUT} = 0.25$ to 5 MW, $n_e = 0.24$ to $6 \times 10^{20}/\text{m}^3$, $\kappa = 0.94$ to 1.85, $\delta = 0.0$ to 0.85, and $a = 0.17$ to 0.24. The principal

*E-mail: g@psfc.mit.edu

heating scenario employed is first-harmonic hydrogen in a deuterium majority plasma at 5.3 T and an ICRF frequency near 80 MHz. The same frequency is used for heating a ^{3}He minority at 7.9 T. Half of the rf power is available from sources tunable from 50 to 80 MHz, expanding the range of toroidal fields that can be efficiently heated. Second-harmonic deuterium majority and mode conversion heating scenarios have also been exploited. Details of the ICRF systems and results can be found in Ref. 1.

C-Mod operation has several unique features with respect to transport studies. Because the B/R ratio is high, the machine typically runs at densities that are 10 times higher than those of conventional tokamaks. This extends operation to higher collisionality and lower fast-ion content and leads to the reactor relevant condition of equilibrated electrons and ions in most regimes. The exclusive use of rf and ohmic heating allows the study of transport in discharges with no core particle or momentum source. While C-Mod operates in a unique dimensional parameter range, it can be run so as to overlap in dimensionless parameters with larger low-field tokamaks. This combination allows us to

1. dramatically extend the range of engineering parameters in global scaling studies
2. perform dedicated dimensionless identity experiments in which all dimensionless parameters are held fixed between two or more machines
3. perform dimensionless scaling experiments in which one dimensionless parameter is scanned over a wide range between two or more machines with other dimensionless parameters held fixed
4. extend physics studies to unique regions of dimensionless parameter space.

C-Mod has a strong diagnostic set for transport studies that is described in detail in Ref. 2.

Alcator C-Mod addresses a broad range of transport issues, emphasizing those areas where it has unique capabilities, is in unique parameter regimes, observes unique or unusual phenomena, or can make important comparisons with other devices. Comparisons with theory and modeling form an important part of the program, with theory playing a critical role in motivating experiments and in determining their design. This paper covers only global and local transport studies in ohmic, L-mode, and H-mode plasmas, with emphasis on the latter. Work on the H-mode has included studies of local threshold conditions and comparisons with theory, demonstration of regimes with good confinement but no large, potentially destructive edge-localized modes (ELMs), links between core and edge confinement and connections to theoretical models of marginal stability, and dimensionless scaling of the core and pedestal plasma profiles. Other papers in this issue discuss impurity transport,[3] momentum transport,[4] H-mode pedestal and threshold physics,[5] and internal transport barrier regimes.[6]

II. CONFINEMENT IN OHMICALLY HEATED PLASMAS

Ohmic plasmas have been studied over a wide range in plasma current (I_P = 0.24 to 2.0 MA), toroidal field (B_T = 2.0 to 8.0 T), plasma density (n_e = 0.24 to 6 × 10^{20}/m^3), plasma shape (κ = 0.94 to 1.85), and size (a = 0.17 to 0.24). While the heating power is applied only in the electron channel, for all but the lowest-density C-Mod discharges, the electron-ion heat exchange is fast, and significant power flows through the ion channel as well. Ohmic plasmas have a low β (0.1 to 0.5%), large normalized size $1/\rho^*$ (200 to 500), and a wide range of collisionality (0.04 to 4.5). The central electron temperature $T_e(0)$ in these discharges ranges from 700 to 3500 eV. Confinement properties are studied mostly by analysis and integration of plasma density and temperature profiles. [At the very low β_P that is typical of ohmic discharges, the magnetohydrodynamic (MHD) analysis of the stored energy can be burdened by significant systematic errors. For discharges with auxiliary heating, where both methods are valid, the agreement is excellent—typically within 10%.] Four distinct confinement modes are observed. At very low densities the Alcator or linear ohmic confinement (LOC) regime is recovered in C-Mod. This regime, which was first discovered on Alcator A (Ref. 7), has the energy confinement time τ_E proportional to plasma density. At all other densities (which encompasses most operations), ohmic discharges are in the saturated ohmic confinement (SOC) regime, where energy confinement is independent of density. Confinement scaling and transport properties of these discharges are essentially indistinguishable from auxiliary heated L-mode plasmas and may properly be called "ohmic L-modes."[8] When the plasma current is raised and/or the toroidal field is lowered such that q_{95} approaches 2.5, ohmic H-modes are produced. These discharges are similar to auxiliary heated H-modes, but because of the low heating power, they remain close to the L/H threshold and tend to be transient and to have only moderately improved confinement. Ohmic discharges can also develop internal transport barriers (ITBs). Most ohmic H-modes develop this feature spontaneously if the H-mode is sustained for more than a few confinement times.[9] Ohmic ITBs are also produced by pellet injection.[10,11]

II.A. Linear Ohmic Regime

The LOC regime occurs only in a narrow range of densities, very roughly in the range of 10 to 20% of the density limit. This range is bounded on the lower end by the appearance of runaway electrons or locked modes[12] and by confinement saturation on the upper end. The saturation point can be characterized on C-Mod by

$n_{20} \sim 4/q$, where n_{20} is the line-averaged plasma density in $10^{20}/m^3$ and q is the MHD safety factor. Sufficient data to reliably scale the saturation threshold do not exist however. Figure 1 shows the energy confinement time versus density for a set of data at fixed toroidal field and current. For the standard shape, with $k \sim 1.5$, the break between regimes is observed at approximately $n_e \sim 0.6 \times 10^{20}/m^3$. Regressions using a larger set of data (with major radius fixed) give

$$\tau_E = 0.156 n_e^{0.95} a^{2.1} q^{1.2} \quad ,$$

where τ_E is in seconds, n_e is in $10^{20}/m^3$, and a is in meters. The fit is shown in Fig. 2a. The size scale is not reliable because of the narrow range of data, so this result is reasonably close to the so-called neo-Alcator scaling $\tau_E = 0.066 n R^2 a \kappa^{0.5} q$ (Refs. 7 and 13), with which the data are compared in Fig. 2b. The observed scaling with nq also helps to explain why the neo-Alcator regime is more restricted in modern machines. With their stronger shaping, the increase of confinement with density is so rapid in these devices that it quickly reaches the L-mode levels and saturates.

It seems clear from the higher elongation data in Fig. 1 that the linear and saturated confinement laws do not add in quadrature as early authors had suggested.[13] The sharp transition suggests instead proximity to marginal stability. Careful transport analysis with the TRANSP code[14] shows that for these low-density plasmas, the loss channel is indeed in the electrons, and that the ions are conducting a negligible fraction of the power. The saturation seen at higher densities can be understood as the appearance of ion turbulence that is driven when the ion heat flux becomes difficult to carry via collisional transport.[15] A useful way of looking at the break between regimes is that as the plasma density and safety factor are lowered, a new electron loss channel opens up, conducts all available power, and reduces the ion heat flux, allowing it to drop to neoclassical levels. This interpretation was supported by the TRANSP analysis. At high densities, peaking the density profiles stabilizes the ion channel (by lowering $\eta_i \equiv L_n/L_T$) and allows the neo-Alcator regime to be extended.[16]

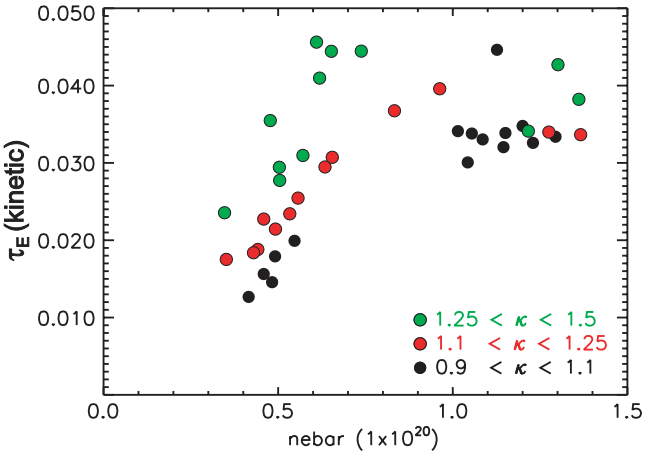

Fig. 1. Energy confinement time τ_E is plotted against density for discharges with ohmic heating alone. The dependence on elongation is in part a manifestation of the q scaling in the linear regime. For standard plasma shapes, $k \sim 1.5$ or higher, the linear confinement (Alcator) regime is obtained only at densities below $\sim 6 \times 10^{20}$.

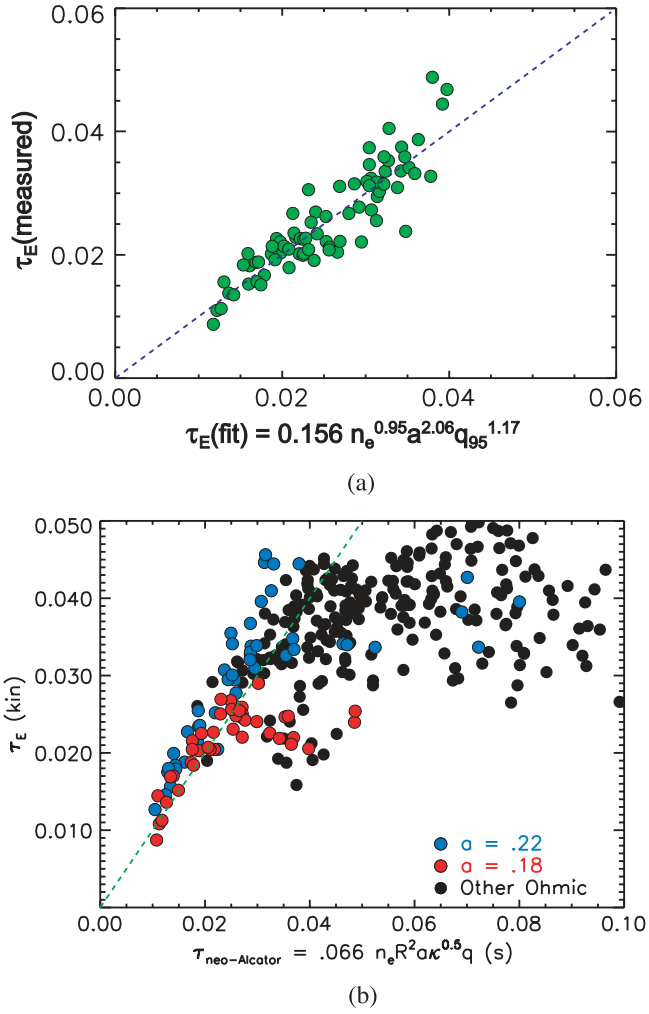

Fig. 2. (a) Power law regression for confinement data from the LOC regime. (b) Ohmic confinement data plotted against the neo-Alcator scaling law. Reasonable agreement is obtained in the low-density regime. The blue and red points correspond to a set of dedicated scans.

II.B. Saturated Ohmic Regime

As the plasma density is raised, the ohmic power is coupled to the ions and the density dependence of the energy confinement disappears. An unconstrained

regression to saturated ohmic C-Mod data is shown in Fig. 3a and yields[8]:

$$\tau_E = 0.039 I_P^{0.98} n_e^{0.12} m^{0.24} P_{OH}^{-0.60} \quad .$$

The covariance between ohmic power and current has long been noted, limiting the reliability of such scalings. However, the resemblance to standard L-mode scaling derived for experiments with strong auxiliary heating is striking. The ohmic data can also be compared to this scaling law and as shown in Fig. 3b, yield reasonable agreement. The distinction between the saturated ohmic regime and L-mode is probably not a useful one.

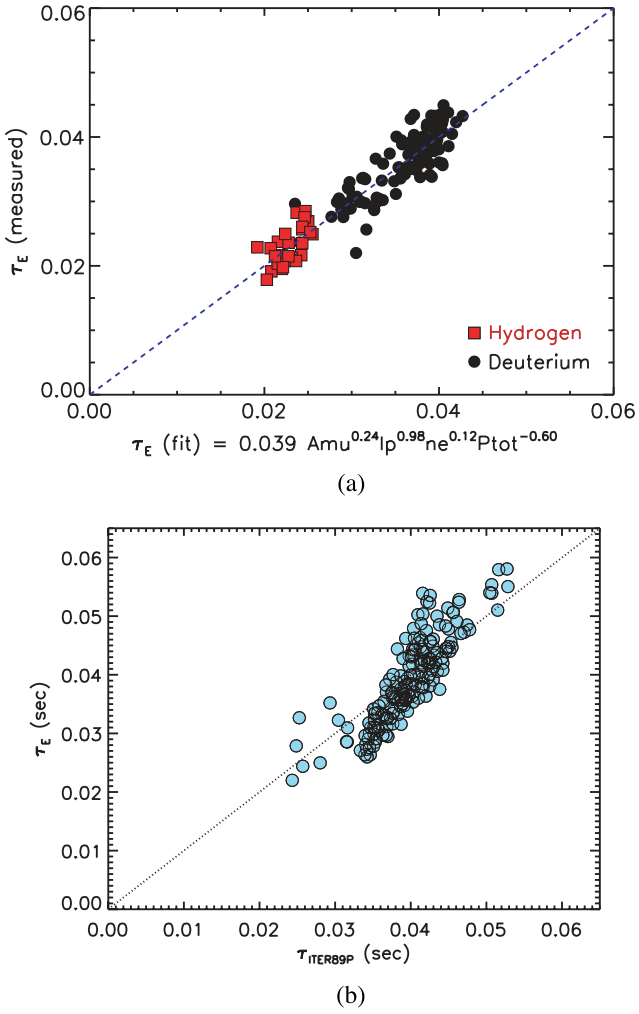

Fig. 3. (a) Power law regression for confinement data from the SOC regime. (b) Ohmic confinement data from the SOC regime plotted against the predictions of the ITER89 L-mode scaling law.

III. L-MODE CONFINEMENT IN AUXILIARY HEATED PLASMAS

Using the ICRF systems described in Ref. 1, input powers have been raised to 5 MW, resulting in ion and electron temperatures as high as 6 keV. The resonant nature of ICRF heating constrains the values of B_T for which efficient heating can be achieved. However, by employing various scenarios (D/H minority, D/^{3}He minority, second-harmonic D majority, ^{3}He/D mode conversion) and various rf frequencies (50, 70, and 80 MHz), experiments with auxiliary heating have been carried out in C-Mod from 2.8 to 8 T. The range of values for plasma current, density, and shaping are similar to those described in Sec. II. Because of the high densities employed, ion tails produced by minority heating are well coupled to the bulk and seldom account for more than 5 or 10% of the stored energy. Under most conditions, low-Z impurities tend to be unimportant and Z_{eff} is not far above 1 (Ref. 8). Assuming an L-mode–like scaling for impurity confinement, this is equivalent to $(Z_{eff} - 1)$ proportional to energy/particle. Fitting the available confinement data yields for L-mode plasmas, including the SOC data, leads to the following[8]:

$$\tau_E = 0.023 I_P^{0.96} n_e^{-0.10} m^{0.15} B_T^{0.29} \kappa^{0.45} P_{TOT}^{-0.50} \quad .$$

Figure 4a shows the results of this regression. Comparison with the ITER89 scaling law[17] is shown in Fig. 4b.

IV. H-MODE

IV.A. Introduction, L-H Transition, and Thresholds

Access to H-mode was a critical concern when Alcator C-Mod was under construction, with predictions for the power threshold at the time ranging from 0.1 to 10 MW (Ref. 18). When the machine operated, the L/H threshold was found to be in the range of 1 to 2 MW (Ref. 19). By extending the range in density and field by significant factors, the C-Mod results helped put the threshold scalings on a much firmer basis.[20] Because of the all-metal first-wall construction and the need to control high-Z impurities, good-quality, sustained H-modes were not achieved until the machine was boronized[21]; however, neutral control via wall conditioning was not an issue in C-Mod. The L/H power threshold was found to scale linearly with nB above a low-density limit that was in the range 0.7 to 0.9 $\times 10^{20}$ for typical operating conditions of 5.3 T and 0.8 to 1.0 MA (Ref. 22). As discussed above, H-modes could be produced with ohmic heating alone, at higher currents (to maximize ohmic power) and at low toroidal field (to minimize the threshold).[23] Significant hysteresis in the H-mode thresholds was observed, with H/L transitions occurring at less than half the power of forward transitions. Perhaps of greater interest were studies of the threshold based on local edge parameters where transitions occurred when a critical temperature (or temperature gradient) was crossed in

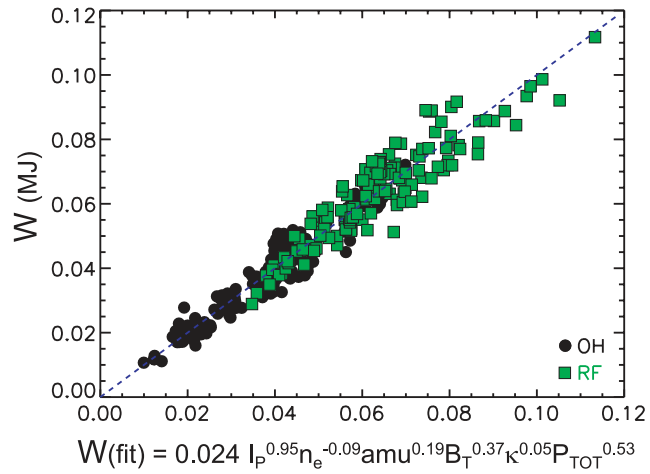

(a)

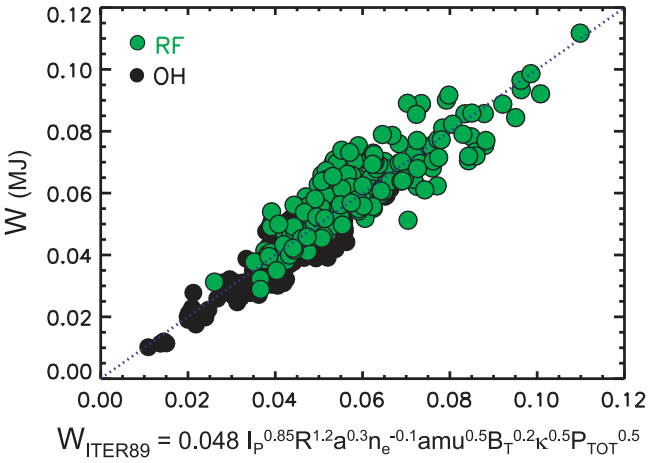

(b)

Fig. 4. (a) Power law regression of C-Mod L-mode confinement data, showing the strong scaling with plasma current and input power that is typical of that regime. (b) The L-mode data compared with the ITER89 L-mode scaling law.

either direction.[24] The critical temperature was seen to scale with B_T, having a value of about 140 eV at 5.3 T (Ref. 25). These results are roughly consistent with the transition theories of Guzdar et al.[26] The total power and critical temperature for the transition was roughly a factor of 2 higher in discharges where the ion ∇B drift was directed away from a single null x point compared to discharges with the drift toward the x point. Recent studies suggest that this can be explained by flows driven in the scrape-off layer (SOL) by poloidally asymmetric cross-field transport.[27] Details on L/H threshold studies can be found in Ref. 5. L/H transitions are rapid in C-Mod, with dramatic drops in edge fluctuations occurring in 50 to 100 μs (Ref. 21).

IV.B. H-Mode Regimes

H-modes have been studied in C-Mod over a wide range in plasma current (0.4 to 1.2 MA), toroidal field (2.6 to 7.9 T), plasma density (1.5 to $5.0 \times 10^{20}/m^3$), and plasma shape ($1.55 < \kappa < 1.85$; $0 < \delta < 0.80$) and with rf powers up to 5 MW (Ref. 21). In terms of the Greenwald density limit, H-modes have been studied at $n/n_G = 0.3$ to 0.85 [n_G is the tokamak density limit, equal to $I_P/\pi a^2$ (Ref. 28)]. The highest-performance H-modes have densities above $4.0 \times 10^{20}/m^3$ and electron and ion temperatures above 4 keV, yielding peak and average pressures of 0.53 and 0.18 MPa, respectively. These are perhaps the highest volume-averaged plasma pressures ever produced in a magnetic confinement experiment. Pedestal temperatures range from 200 to 1000 eV. Density profiles in these H-mode plasmas are quite flat, except in cases where ITBs develop, and Z_{eff} tends to be low, ranging from 1.0 to 2.5. An unexpected feature of these torque-free, rf-heated discharges is strong cocurrent rotation, up to 100 km/s for high-performance H-modes.[29]

As in other devices, various H-mode regimes are observed in C-Mod, and they correspond principally to different edge relaxation mechanisms.[30] When the conducted power is just above the threshold and the edge temperature is low, type III ELMs are seen.[31] These are often regularly spaced, repeating at 1 to 5 kHz, with each individual ELM having no discernible effect on the core plasma and causing only minimal perturbation to the pedestal. The overall confinement properties of these discharges are poor. At higher pedestal temperatures, the type III ELMs disappear and two types of H-modes can exist. With higher currents and/or with weak shaping, the plasmas tend to be ELM-free. This regime is always transient, with particles and impurities accumulating, leading to a back transition. With stronger shaping or at lower plasma current, high-performance, steady discharges can develop. The discharges are characterized by high levels of recycling light and have been termed enhanced D_α (EDA) H-modes.[32] While technically free of ELMs, the EDA plasmas are similar in most other respects to type I ELMy discharges commonly found in other devices. However, in the case of EDA, the pedestal is regulated by a continuous quasi-coherent (QC) oscillation in the range of 50 to 200 kHz (Refs. 33 and 34). Figure 5 shows the comparison between an ELM-free and an EDA discharge. Most notable is the dramatic drop in radiated power for the EDA case, along with its steady density and stored energy. As the pedestal pressure is raised further (corresponding to the global $\beta_N > 1.2$), small, "grassy" "type II" ELMs appear.[34] These can coexist in EDA discharges, as shown in Fig. 6. At still higher pedestal pressures and at somewhat lower densities, these small ELMs predominate and the QC mode disappears. The type II ELMs can be seen as minor perturbations in the edge pedestal and SOL particle flux; however, individual ELMs

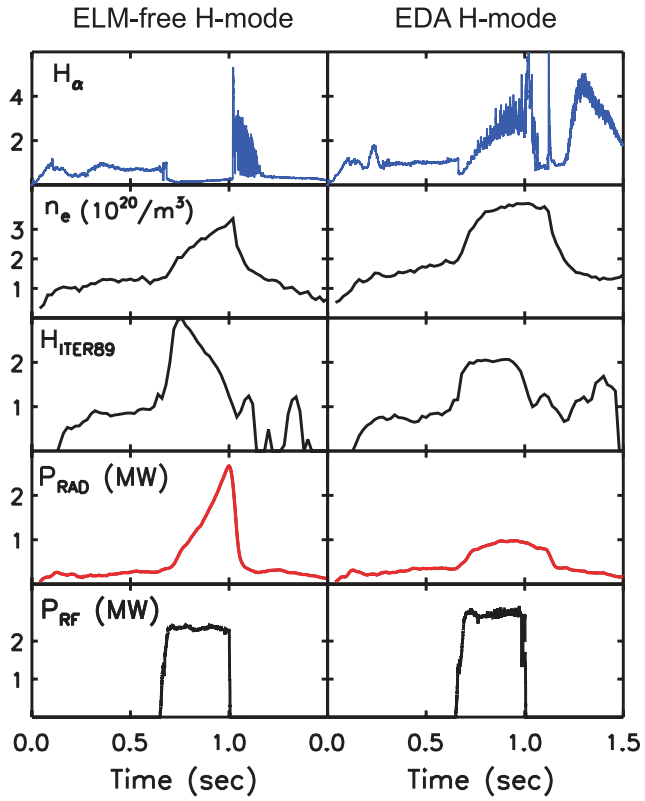

Fig. 5. Comparison of ELM-free and EDA discharges. The only significant difference in the target plasmas is the slightly lower target density for the ELM-free case. However, a sharp drop in particle confinement is inferred from the density and radiated power traces for EDA. The result is a steady discharge with good energy confinement.

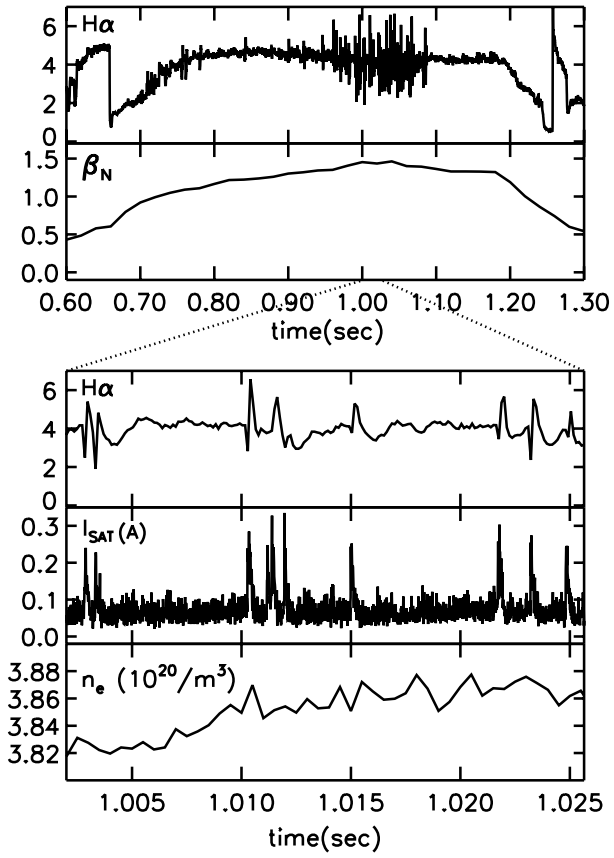

Fig. 6. At higher pedestal pressures, small ELMs can be seen superimposed on the EDA plasmas. While individual ELMs are visible on H_α and divertor probes (I_{SAT}), no drop in global stored energy or line-averaged density can be discerned.

have no discernible effects on global parameters such as stored energy or line-averaged density. They do not correspond to a destruction or severe degradation of the pedestal. As discussed below, unlike the EDA or type III discharges, the pedestals of these plasmas have pressure gradients near or above the ideal stability limit. Type I ELMs, which do transiently destroy the edge pedestal and which can be seen individually on global parameters, *have not been seen in C-Mod*. In a very few unusual discharges, large discrete ELMs are observed, but even these do not seem to have the character of type I ELMs. Thus, the "standard" H-modes for C-Mod are EDA or those with type II ELMs. While uncommon on other devices, the EDA regime is apparently not entirely unique to C-Mod. In early JET experiments, a regime dubbed LPC for low particle confinement was observed.[35] This mode has not been produced since, so direct comparisons are not possible; however, in most respects it appears to be similar to EDA. Dimensionless identity experiments, carried out between C-Mod, ASDEX-Upgrade, and DIII-D, found that in cases where the dimensionless parameters of those machines matched C-Mod EDA plasmas, some signatures of the EDA regimes were observed.[36] JFT-2M has recently reported an HRS (for high-recycling steady) H-mode regime, which also shares many of the same characteristics.[37] The HDH (high-density H-mode) regime seen on the W7AS device also has common features.[38] Further details on the confinement properties of and the boundaries between the H-mode regimes are discussed below. Descriptions of the pedestal profiles and scalings can be found in Ref. 5.

IV.C. EDA and Small-ELM H-Modes

The EDA and small-ELM regimes are of particular importance because they combine good energy confinement and moderate particle and impurity confinement (and thus a potential for steady-state operation) without large power or particle impulses to the divertor, as is the case for large-ELM regimes.[34,39] Energy confinement in these regimes is typically 80 to 90% of that of ELM-free operation[21,34] (that is, in the early phase of ELM-free

TABLE I

Summary of EDA and ELM-Free H-Mode Features

	ELM-Free H-Mode	EDA H-Mode
Energy confinement	$H_{89} \sim 2.1$	$H_{89} \sim 1.9$
Particle confinement	$\tau_I \gg \tau_E$	$\tau_I \sim 2$ to $3 \times \tau_E$
Momentum confinement	Strong inward pinch	Diffusive
Edge fluctuations	None observable	QC fluctuations 50 to 200 kHz
X-ray pedestals	Narrow, 2 to 6 mm	Wide, 4 to 12 mm
Dependence on q_{95}	More likely when $q_{95} < 3.7$	More likely when $q_{95} > 3.7$
Dependence on δ	$\delta < 0.35$	$0.35 < \delta$
Dependence on density and collisionality	Favored at low density and collisionality	Favored at high density and collisionality

operation, before impurity accumulation degrades performance). A general feature of these discharges is an overall increase in the hydrogen Balmer-α light, a decrease in the rate of density rise, and lower levels of impurity radiation, all suggesting increased particle transport. Figure 5 compared some important signals from an EDA (with small ELMs) discharge with those from an ELM-free one. As noted, the lower-level radiated power and steadier confinement of the EDA plasma are significant. The difference in radiation is due to dramatically lower impurity confinement for the EDA case.[21] Impurity transport is discussed in more detail in Sec. VII and in Ref. 3. A summary of features from these regimes is contained in Table I.

Access conditions to the EDA and small-ELM regimes have been extensively investigated.[34,40] Dedicated scans of q (both I_P and B_T), density, power, working gas, and shape (elongation κ and triangularity δ) were carried out. It was found that EDA and ELMy conditions were more likely at higher safety factor ($q > 3.5$), higher triangularity ($\delta > 0.35$), and higher target density. The dependence on triangularity is seen in Fig. 7a, where a continuous scan from high to low triangularity was carried out for otherwise fixed conditions. The discharge showed a series of sharp transitions between the regimes as the triangularity dropped, spending more and more time in the ELM-free regime and finally becoming purely ELM-free. The amplitude of the QC mode precisely followed each of these transitions before disappearing. This phenomenon has the appearance of "dithering" between the EDA and ELM-free regimes. A closer look reveals substantial structure, with dithering behavior consisting of a series of periodic transitions spaced about 1 ms apart. As seen in Fig. 7b, a short burst of the QC mode accompanies each EDA period. Similar results were obtained with scans of the safety factor. No obvious dependence of the EDA/ELM-free boundary on κ or input power was found over the ranges studied. EDA discharges produced in ohmic H-modes (shown in Fig. 8) show the same accessibility boundaries; thus, this regime cannot be attributed to direct effects of rf or of a high-energy minority ion tail.[40] Figure 9 shows the boundary between EDA and ELM-free operation in the q, δ plane. One can see that the boundary is "soft"; that is, there is a good deal of overlap between the two sets of data, suggesting additional dependences. It is also interesting to note that very similar plots have been obtained for access to small-ELM regimes in other devices.[41] Experiments in majority hydrogen plasmas found EDA operation at lower q values, down to 2.6. As the heating power is increased, the plasma pressure increases and small, type II ELMs begin to dominate.[21,34] At higher powers, the QC mode disappears entirely and the plasma is regulated by the small ELMs alone. Figure 6 showed traces from several diagnostics depicting these ELMs. Note that the ELMs are "bipolar" on the Balmer-α traces; that is, the perturbations are above and below the baseline H_α level. Their MHD characteristics are discussed in Ref. 42. Figure 10 shows a boundary between EDA and ELMy discharges in a plot of pedestal temperature versus pressure.[43] It can be seen that EDA tends to be restricted to somewhat lower values of pressures and higher values of collisionality. Results of stability calculations with the ELITE code[44] are also plotted in this figure. Using measured pedestal temperature and density profiles and current profiles computed with comprehensive models for neoclassical resistivity and bootstrap current, it was found that the EDA/ELM boundary corresponded to the stability boundary for intermediate n coupled peeling/ballooning modes.[43]

IV.D. THE QC MODE AND EDA

The connection between the appearance of QC fluctuations and the EDA H-mode seems to be causal. That is, we find that the QC mode is the probable mechanism by which the pedestal profiles and transport are regulated in an EDA plasma. This conclusion rests on three observations. First, the QC mode is always present in discharges that show the other aspects of the EDA regime—high levels of Balmer-α light (relative to

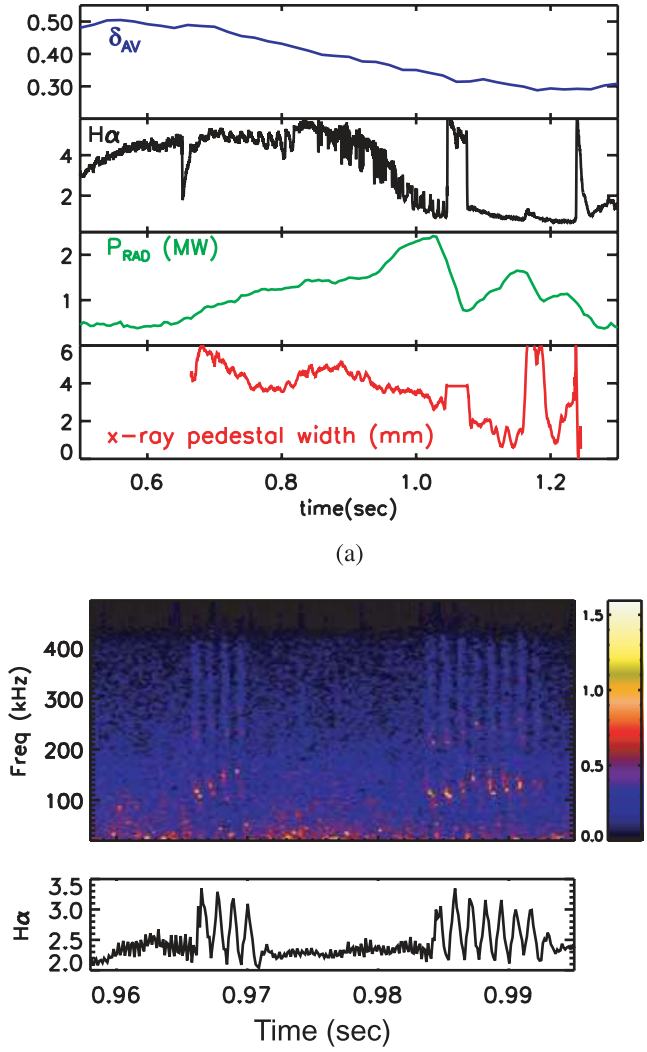

Fig. 7. (a) The dependence of the ELM-free EDA boundary can be seen in this triangularity scan. As δ is lowered, the discharge begins to dither between these two H-mode regimes, finally, as seen by the radiated power curve, losing its H-mode character. (b) On this expanded scale, it can be seen that each dither from ELM-free to EDA is a complex structure consisting of a series of QC fluctuation bursts, each lasting about 0.5 ms.

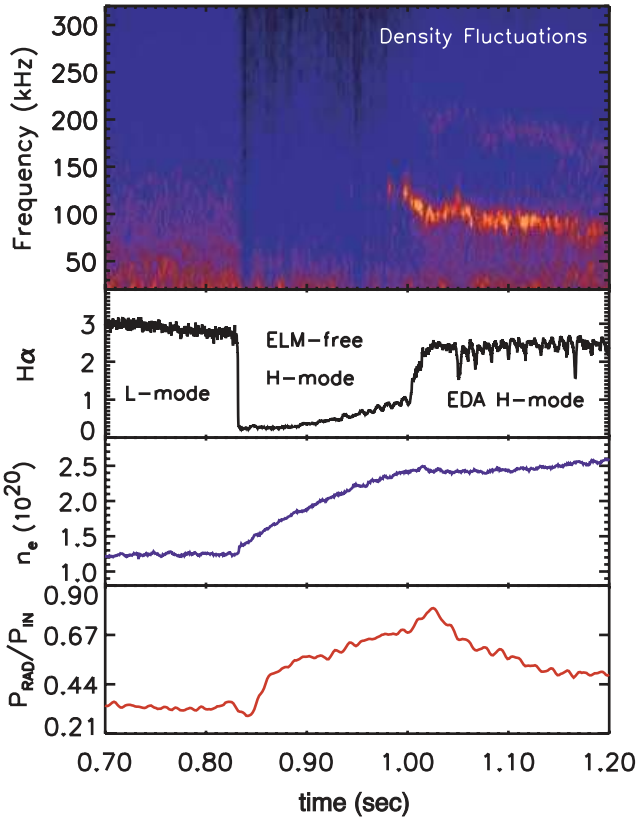

Fig. 8. An EDA H-mode is obtained with ohmic heating alone. The transition from ELM-free to EDA, which was the result of raising q_{95} via a B_T scan, occurs at about 1.0 s and is accompanied by a decrease in impurity content, a drop in the rate of density rise, and the appearance of the QC mode.

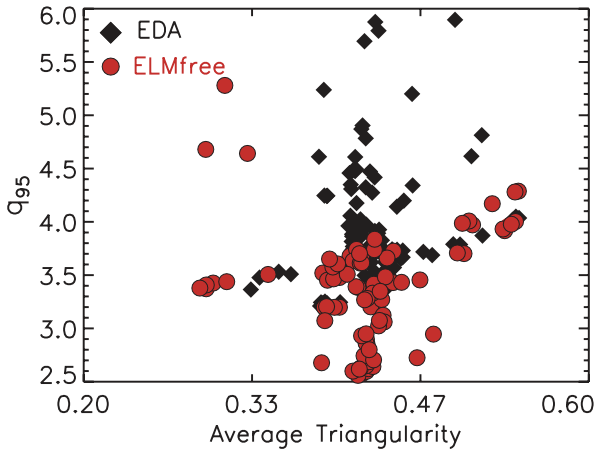

Fig. 9. EDA ELM-free boundary plotted in q-δ space, showing that EDA is more likely at higher safety factor and higher triangularity. There are significant areas of overlap, suggesting that other variables are important as well.

ELM-free H-modes), decreased particle confinement, and sharply increased impurity transport relative to ELM-free H-modes. Second, the mode is localized in the steep gradient region of the pedestal. Third, there is a nearly linear relationship observed between the amplitude of the QC mode and the local particle diffusivity at the separatrix. This latter quantity is determined by using local, high-resolution measurements of the density, temperature, and Lyman-α emission to calculate the ionization source rate across the pedestal and SOL and dividing

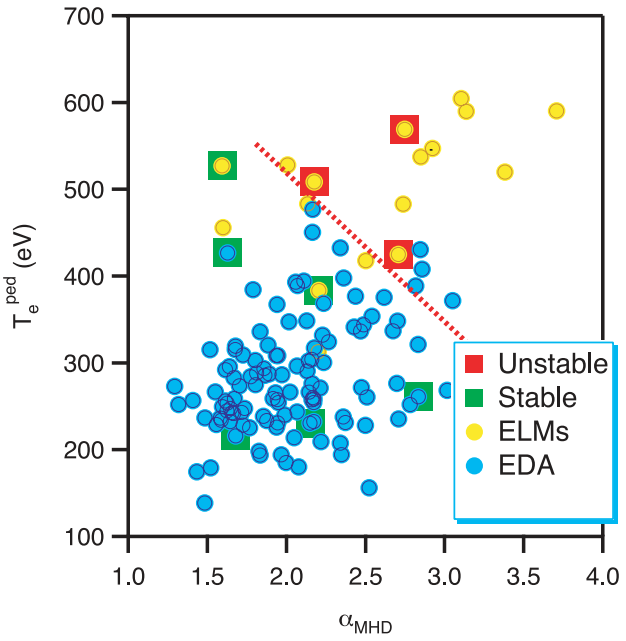

Fig. 10. Boundary between EDA and small, type II ELMs plotted in a space comprised of the edge temperature and the normalized pressure gradient (α_{MHD}). EDA tends to disappear at higher pressures and temperatures. The square symbols denote shots for which MHD stability calculations have been performed. The boundary between regimes seems to be coincident with the stability boundary for intermediate n peeling-ballooning modes.

by the local electron density gradient to get an effective diffusivity. The result of such calculations is shown in Fig. 11. A similar dependence has been observed between the mode amplitude, Balmer-α level, and pedestal

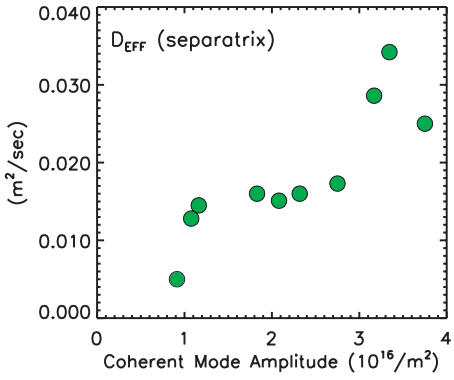

Fig. 11. Effective pedestal particle diffusivity D_{eff} (calculated at the separatrix) plotted against the amplitude of the QC mode. The near-linear relation suggests a causal relationship between the mode and enhanced particle transport.

X-ray width,[45] the latter quantity being a good measure of local impurity transport.

With the importance of the QC fluctuations established, it is worth describing the mode in somewhat greater detail. It was first observed via reflectometry at 88 GHz (Ref. 33), with further measurements by electrostatic probes, electromagnetic probes, phase contrast imaging (PCI), gas puff imaging (GPI), beam emission spectroscopy (BES), and heterodyne electron cyclotron emission (HECE) measurements.[46,47] That is, it can be seen by all diagnostics capable of measuring short-wavelength fluctuations in the plasma edge. The fluctuation amplitude is large, with the local $\delta n/n$ reaching 50%. The electromagnetic perturbation is also significant, with $\delta J/(J_{OH} + J_{BS}) \sim 20\%$, the latter number coming from measurements by a pair of magnetic loops mounted on a fast scanning probe and inserted to within 1 cm of the separatrix.[46] While the magnetic perturbation is large, it is usually not observed by the standard set of magnetic probes mounted on the vacuum vessel wall. Typical spectra of the QC mode can be seen in Fig. 12. The normalized spectral width $\delta f/f$ is approximately 0.1, though this value may vary from 0.05 to 0.3. Figure 13 shows the evolution of the autopower spectra from PCI measurements versus time. It is customary for the QC mode to sweep down in frequency following the L/H transition. This is believed to result from a change in the Doppler shift that occurs as the H-mode pedestal is established. The mode frequency decreases as the pedestal pressure gradient (and core rotation velocity) increases, and the fluctuations have a phase velocity of approximately 1.5 km/s in the electron diamagnetic direction. The mode has a relatively short wavelength. Figure 14 shows an intensity plot in ω, k space taken from PCI data.[48] Diagnostics capable of measuring the wavelength of the mode cover a range of poloidal locations. These results are summarized in Fig. 15, where poloidal wave numbers obtained from PCI, GPI, and probes are plotted versus poloidal field angle. The solid line shows the expected result for a field-aligned perturbation. The short poloidal

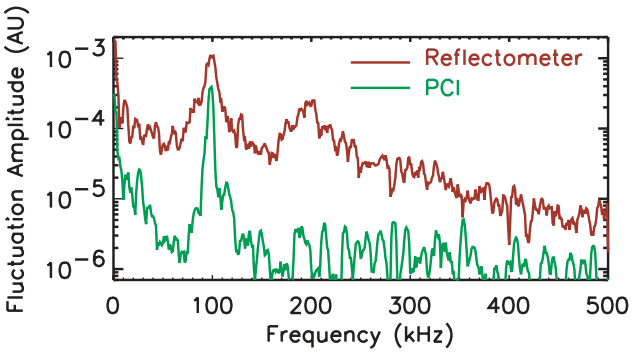

Fig. 12. QC mode autopower spectra plotted for data from the PCI and reflectometry diagnostics.

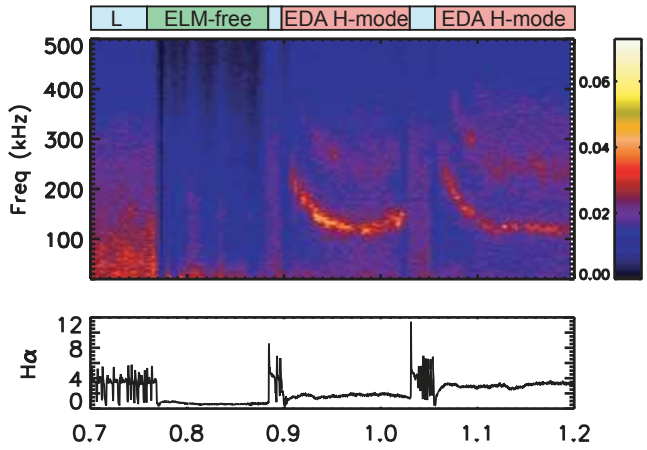

Fig. 13. The evolution of the QC mode spectra, showing strong downward sweeps in frequency following each transition, can be seen in a discharge with three distinct H-mode periods. The change in frequency is believed to be from Doppler shifts that arise as rotation builds up in the pedestal.

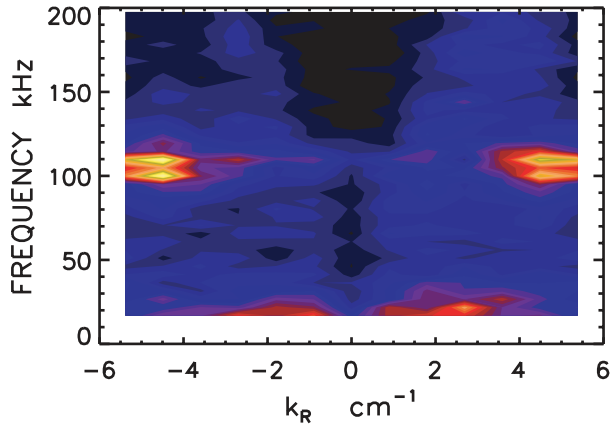

Fig. 14. Wave number–resolved spectra of the QC mode from the PCI diagnostic, showing well-defined mode structures. The positive and negative features correspond to the top and bottom of the machine, which are traversed by the PCI beam.

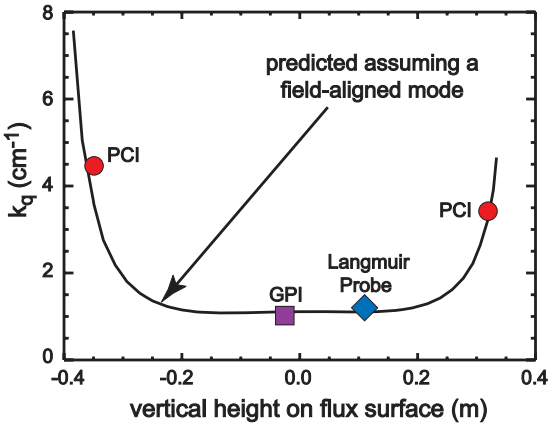

Fig. 15. Wave number of the QC mode from a number of diagnostics compared to the predictions for a field-aligned perturbation, showing good agreement.

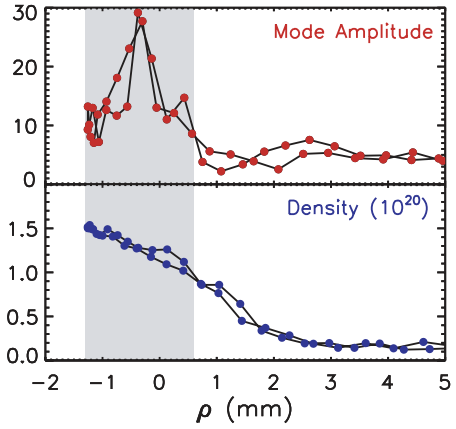

Fig. 16. QC mode amplitude, taken from scanning probe data, plotted against radius. From this measurement, a mode width of 1 to 2 mm is inferred. The shaded region represents the separatrix with uncertainty from the equilibrium mapping.

wavelength explains why the mode is hard to observe with standard magnetic pickup coils. Localization of the mode can be achieved by the BES, GPI, reflectometry, and probe data. The mode has a radial extent less than 4 mm, perhaps as small as 1 to 2 mm, and is located just inside the separatrix,[49] as seen in Fig. 16. Similar fluctuations have been seen between ELMs in H-mode discharges on other devices: PDX (Ref. 50), CCT (Ref. 51), PBX (Ref. 51), and DIII-D (Ref. 52).

The appearance of coherent modes in a region with pressure gradients near the MHD stability limits and at high collisionality suggests a connection to resistive ballooning. These modes should be destabilized at higher values of $q/m_i^{0.5}$, in qualitative agreement with the EDA threshold studies.[53] While these modes are found to be turbulent if driven far beyond their linear threshold, coherent modes, saturated by quasi-linear flattening of the profiles, have been found in simulations.[54] Three-dimensional, electromagnetic fluid codes [DRB (Ref. 55) and BOUT (Ref. 56)] have been used to simulate the C-Mod edge plasma. Modes very much like the QC mode were produced and matched the experimental observations in several important ways,[48,55,57] most notably the mode localization and wave number. The three-dimensional gyrokinetic code gs2 (Ref. 58) also found a strongly growing linear mode in the pedestal. The lack of ELMs in these discharges may be partially explained by

the high pedestal collisionality ($\nu^* > 1$). This will tend to suppress the bootstrap current, reducing the drive for current-driven modes (peeling), and will destabilize pressure-driven modes like resistive ballooning. Even accepting this explanation for the QC mode, several important questions remain. First, it is far from clear what saturates this very large amplitude mode, or what prevents it from spreading in k space and generating broadband turbulence. Second, we do not understand the feedback loop between the mode and the profiles, which would be the mechanism by which the pedestal is regulated in the absence of ELMs leading to an ELM-free steady-state. Finally, we do not understand why the mode is so effective in transporting impurities relative to plasma energy. New edge diagnostics, which are under construction and include a direct measurement of temperature fluctuations that can be made simultaneously with density and potential fluctuations, along with more extensive modeling may help answer these questions.

IV.E. H-Mode Global Confinement

Energy confinement in C-Mod H-modes provided a test of the global scaling laws developed earlier by international collaborations working on performance projections for ITER (Ref. 59). In these studies, a database of ELM-free H-modes was carefully assembled, screened for known adverse effects (e.g., high levels of radiated power or MHD fluctuations), and fit to a power law equation. The important fitting parameters included plasma size, density, current, power, toroidal field, and elongation, "engineering" variables that can be directly controlled by machine design or operation. C-Mod H-mode data, which became available in 1996, exceeded the ITER93 H-mode confinement predictions, outside the rms errors of the published regression.[21] The C-Mod data averaged about 2 to 3 standard deviations above the fit. The likely cause for the failure to predict C-Mod results was the limited parameter range of the data used for the fit, compared to the extrapolation to C-Mod parameters, and correlations between independent parameters in the database. Following this exercise, data from C-Mod (and additional data from other machines) were included in the international database and the regressions recalculated. The emphasis at this time was on scaling of thermal energy confinement in ELMy discharges, for which C-Mod included EDA and mixed EDA/type II ELMy plasmas. Because of its high plasma density, fast-particle content was relatively low for C-Mod, with nonthermal energy typically 5 to 10% of the total. The results were the ITER97 and ITER98 H-mode scaling laws, which fit the C-Mod data reasonably well.[60] Figures 17a and 17b show comparisons of C-Mod data with the earlier and later scaling laws. The improvement in database conditioning also resulted in fits that were very close to being dimensionally correct without imposition of external constraints.[61]

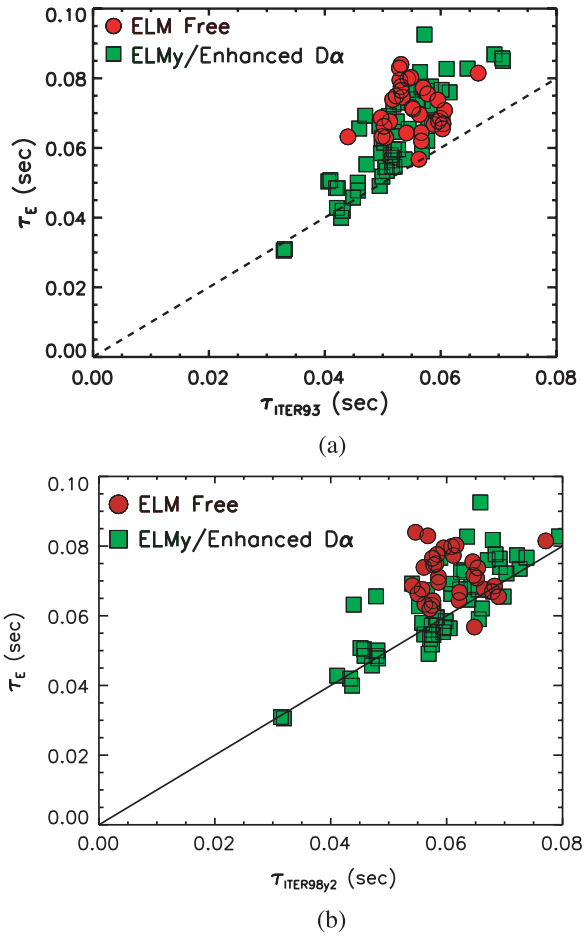

Fig. 17. (a) H-mode confinement data from C-Mod are significantly above the predictions of the ITER93 ELM-free scaling law, which was derived prior to C-Mod operation. Note that the scaling line should be compared primarily to the circles. (b) After C-Mod data were added to the international database and the regressions recalculated, the agreement improved. Note that the scaling line should be compared primarily to the squares.

H-mode confinement can show considerable variability, even for plasmas with nominally similar control parameters. A series of experiments on C-Mod was performed to investigate this phenomenon.[21] Perhaps the most important "hidden" variable for H-mode performance on C-Mod is the level of radiated power. Figure 18 shows the confinement enhancement (H factor) relative to the ITER89 L-mode scaling for a set of discharges over a range of radiated power fraction $f_{RAD} = P_{RAD}/P_{TOT}$. The confinement of L-mode discharges is found to be independent of f_{RAD} across the entire range of data, which includes, within experimental errors, $f_{RAD} = 1$. Part of the explanation for this is that much of the radiated power originates in the outer regions of the plasma, and therefore substantial power is still conducted

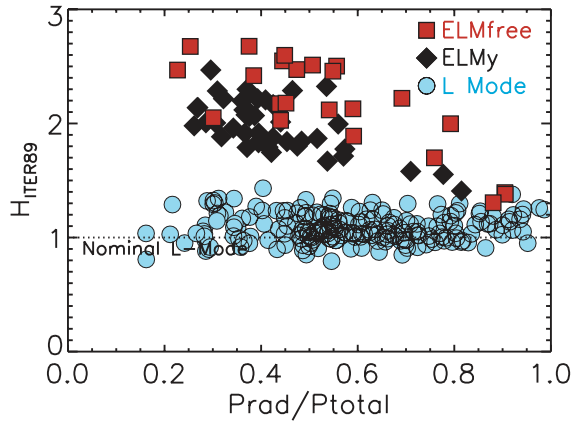

Fig. 18. Confinement enhancement factor H_{ITER89} plotted against $f_{RAD} \equiv P_{RAD}/P_{TOTAL}$ for both L- and H-mode discharges. The L-mode confinement is seen to be insensitive to this parameter, while confinement in the H-mode plasmas drops when f_{RAD} rises above 0.5.

within the plasma interior. In contrast, H-mode confinement deteriorates when the radiated power fraction rises above 50%. As f_{RAD} approaches 1, the H factor also approaches 1; that is, strongly radiating H-modes show L-mode–like confinement, though these discharges still have discernible, though small, edge pedestals. The role of marginal stability and critical gradients for this effect is discussed in Sec. VI. The effect of impurity radiation, particularly from the high-Z wall material, molybdenum, helps to explain the importance of the boronization treatment in achieving good-quality H-modes in C-Mod.[21] Figure 19 shows a comparison of the radiated power profile for H-modes obtained before and after boronization. The sharp increase in absolute level and the shift of radiation into the core for the unboronized discharge is dramatic. A similar story holds for neutral pressure, though the effects are not quite as clear-cut. Good H-modes generally had divertor pressures below about 40 mTorr and midplane pressures below about 0.3 mTorr. Another effect of the divertor is to allow the separatrix temperature to rise in H-mode by increasing the connection length to the first wall. Experiments on other devices had found that minimum gaps on the order of 1 to 2 cm between the separatrix and first wall were necessary to obtain good confinement.[62] On C-Mod, a scan of the outer gap distance showed no effect down to gaps of about 2 mm (Fig. 20). This is approximately the scrape-off length for C-Mod.[63] H-modes obtained in limited discharges, that is, with zero gap, had L-mode–like confinement.[64] A final question addressed in these experiments was the requirement for high input power relative to L-H threshold power in obtaining good confinement. Figure 21 shows the confinement enhancement factor plotted against the ratio of input power to threshold power. The threshold power is taken from an early ITER scaling analysis.[65] While good confinement is obtained at powers close to threshold, one must understand that the threshold is computed based on parameters in the fully developed H-mode. That is, one must have a "reserve" of input power to account for the increase in density following the transition, typically a factor of 2 to 4, over the density of the target plasma.

V. LOCAL TRANSPORT

Values of effective thermal diffusivity χ can be extracted via power balance analysis of the experimental

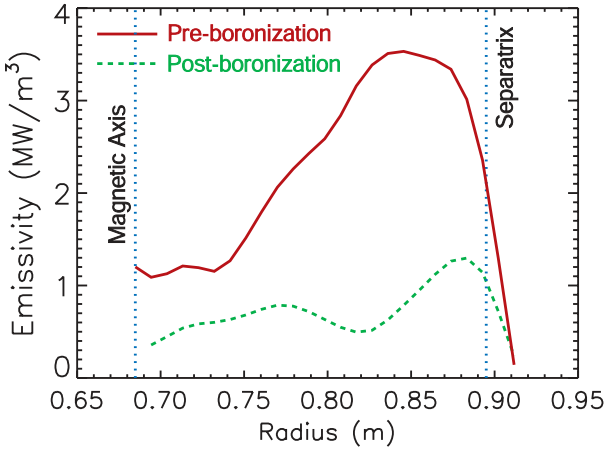

Fig. 19. Profiles of radiated power taken before and after boronization, indicating a dramatic drop in high-Z impurity content following the wall treatment.

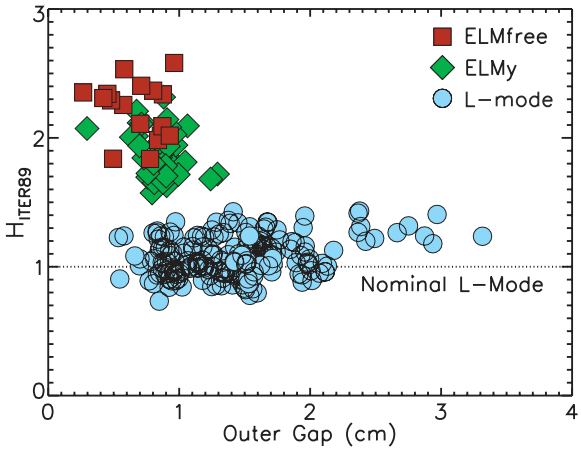

Fig. 20. H factor plotted against outer gap, showing that confinement does not deteriorate if the plasma wall spacing is larger than 2 to 3 mm. This distance roughly corresponds to the SOL width. H-modes were not obtained in discharges limited on the outer wall.

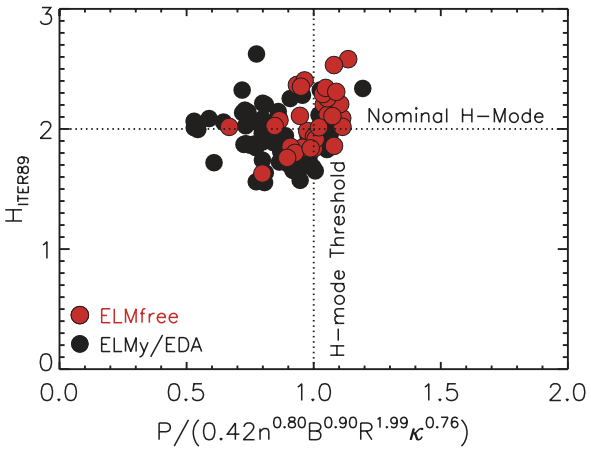

Fig. 21. H factor plotted against $P/P_{THRESHOLD}$. Good confinement is achieved if the heating power is at the threshold computed for the fully developed H-mode. It is important to note that this level of input power is two to four times the threshold power as computed for the target plasma.

data. The TRANSP code was used for this purpose since it has incorporated excellent physics modules for ICRF heating (TORIC) and fast-ion thermalization (FPPRF) (Refs. 14, 66, and 67). Typical input data include profiles for electron density, electron temperature, Z_{eff}, radiated power, total neutron rate, and central ion temperature. The plasma boundary was calculated by the equilibrium reconstruction code EFIT (Ref. 68). For ohmic plasmas in the linear confinement regime, the power was all generated in the electron channel and conducted mainly through the electron channel. Neoclassical ion transport was sufficient to account for the much smaller levels of power conducted through that channel. Electron thermal diffusivity χ_e rose from ~0.5 m^2/s into the range 1 to 2 m^2/s as the density was lowered, as seen in much earlier studies[15] and consistent with the observed drop in confinement. The transport channels could also be separated for relatively low density, high-temperature ICRF-heated L-modes ($n_e < 1.5 \times 10^{20}$), where $\chi_e \sim \chi_i = 0.2$ to 1.2 m^2/s in the confinement zone and $r/a \sim 0.3$ to 0.8. The higher values corresponded to stronger heating, consistent with the degradation seen in global confinement with input power. In these cases, where significant ICRF power was deposited in the ions, they were moderately anomalous, with $\chi_i/\chi_{NC} \sim 1$ to 4, though with substantial error bars due to uncertainty in the ion-electron energy exchange term. At higher densities, this uncertainty prevented the separation of the two channels and instead an effective diffusivity $\chi_{eff} \equiv Q/(n_e\nabla T_e + n_i\nabla T_i)$ was calculated (where $Q = Q_e + Q_i$ is the total conducted heat flux). Figure 22 shows a comparison of χ_{eff} between L-mode and H-mode discharges with similar toroidal field, plasma current, density, and power deposition profiles.

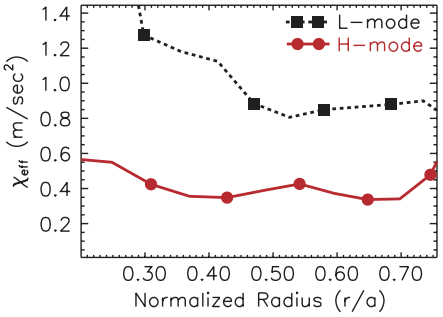

Fig. 22. Effective thermal diffusivity χ_{eff} compared between a matched L-mode and H-mode pair of discharges. The discharges had the same shape, I_P, B_T, P_{RF}, and n_e. The L-mode discharge was taken with reversed field to suppress the transition, despite the strong heating.

The decrease in thermal diffusivity is consistent with the difference in global confinement and demonstrates that the improvement in H-mode confinement occurs across the entire profile, not only in the edge barrier. In general, values and variations in other transport channels, particles, impurities,[3] and momentum[4] reflect variation in thermal transport. Particle transport was measured using a modulated gas puff technique, which allows separation of the diffusive and convective components. Figure 23 shows profiles of these transport coefficients for a typical L-mode discharge.[8] Studies showed that $D_e \sim \chi_{eff} \sim 0.2 - 1.0$ for L-modes.[69] Analogous studies, using transient analysis of impurity content and self-generated plasma rotation, yielded similar results for those channels.[70,71] We note that coupling of transport channels is not universal; when ion transport is suppressed in low-density ohmic or pellet-fueled "P-mode" plasmas, particle transport is also suppressed, but not electron energy transport.[16,72]

Another approach to local transport is via predictive modeling. Physics-based models have been run for C-Mod,

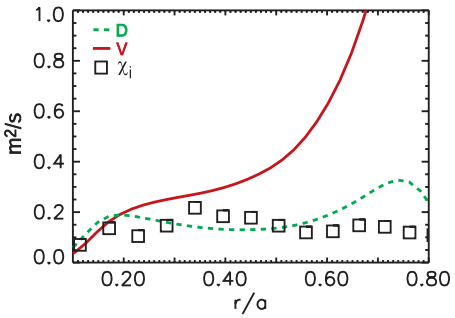

Fig. 23. Particle transport coefficients, calculated from the plasma response to a set of gas puffs, plotted against radius. Note that thermal and particle diffusivity are similar in value.

using input data from the experiment for the equilibrium, heating, and density profile and comparing the calculated temperature profiles with those from the experiment. (Theoretical understanding of particle or momentum transport is still too primitive to allow a meaningful comparison.) The models tested were IFS-PPPL (Ref. 73), GLF-23 (Ref. 74), and the multimode model.[75] These models were all built using results of turbulence simulations or analytic calculations to estimate transport coefficients across a wide range of plasma parameters. Using the measured edge temperature as a boundary condition, these models benchmarked well against larger, lower-field devices,[76] but all models tended to underpredict the C-Mod profiles for both L- and H-modes, typically by about 30 to 40% (Refs. 77, 78, and 79). A typical comparison is shown in Fig. 24. A set of parameter scans and simulations was conducted to try to understand the discrepancy. The conclusion was that the source of the problem was in the linear computation of the critical gradient length for microstability.[80] Nonlinear calculations of this parameter yielded better agreement and are discussed in Sec. VI.

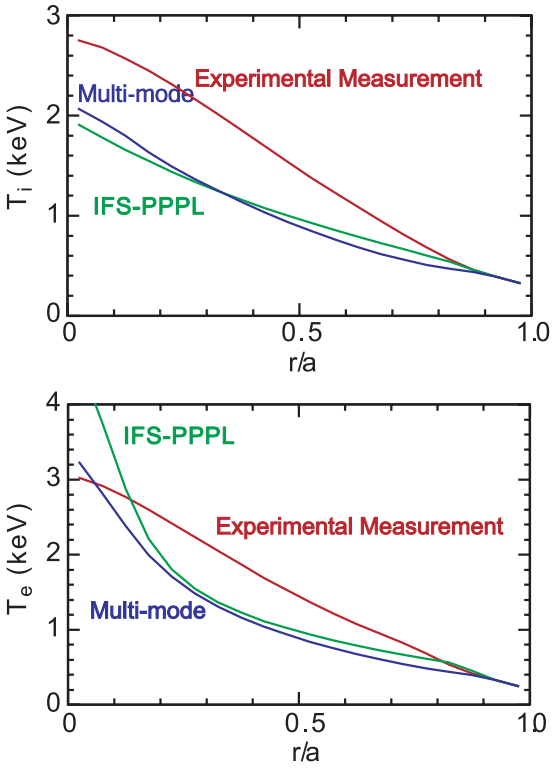

Fig. 24. Measured T_e profiles were found to be significantly above those predicted by several physics-based models. The discrepancy was apparently resolved by nonlinear turbulence calculations. (The upturn in the predicted T_e profiles near the magnetic axis can be attributed to the lack of sawteeth in the models.)

VI. MARGINAL STABILITY AND THE CONNECTION BETWEEN GLOBAL CONFINEMENT AND EDGE TEMPERATURE

The correlation between H-mode performance and pedestal height can be demonstrated by plotting the confinement enhancement factor versus edge temperature, as in Fig. 25 (Ref. 21). The data for this plot correspond to a wide range in heating power but with plasma current only in the range of 0.8 to 1.0 MA. To avoid sensitivity to details of the pedestal profile, the position used for the edge temperature is the 95% flux surface, which is slightly inside the pedestal. What is remarkable about this figure is that it unifies almost the entire C-Mod confinement database (the exception being discharges with peaked density), including L-mode and a wide range of H-mode types and qualities. It shows the quantitative connection between edge and core transport and suggests a direct link between local and global transport. Since the density profiles are relatively flat for these discharges, the proportionality suggests a strong correlation between edge and average temperature. This is confirmed by Fig. 26, which shows a series of temperature profiles for L- and H-mode discharges. The temperature axis is plotted on a log scale, emphasizing the self-similarity of the profiles. If the temperature is given anywhere, it is defined everywhere. These results are summarized in Fig. 27, where the core temperature gradient is plotted against edge temperature[21] and provides an explanation for the so-called "enhanced L-mode."[81] In these discharges, high power, well above the normal L-H threshold, is applied to plasmas that are prevented from entering H-mode by their topology. The confinement improvement can be understood as a consequence of increasing the edge temperature by brute force without the aid of an edge transport barrier. Figure 28 shows a plot of the edge temperature versus power per particle. The benefit of the H-mode transport barrier is that it allows production of high edge

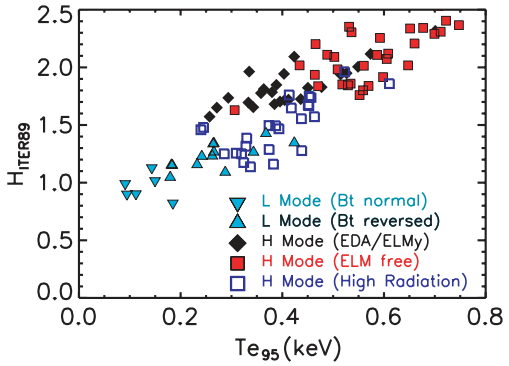

Fig. 25. The confinement enhancement factor H is seen to be tightly correlated with the pedestal temperature across confinement regimes.

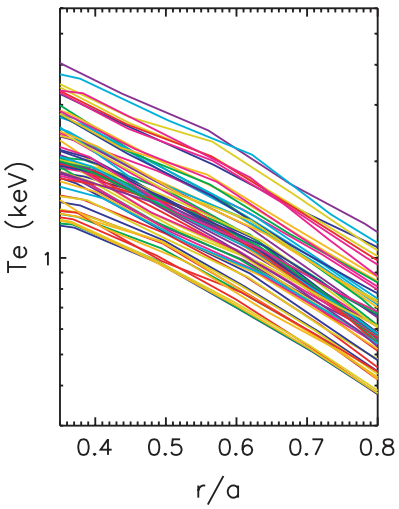

Fig. 26. Temperature profile self-similarity (with the local gradient proportional to the local value) is demonstrated here in a semilog plot of profiles using data from 100 shots chosen randomly from the 2003 and 2004 experimental campaigns. The data were restricted to steady, sawtoothing discharges at 1 MA and 5.3 T, to hold the magnetic shear approximately constant. For consistency, data are plotted at the top of each sawtooth nearest the random time chosen. Otherwise, the data contain all powers and plasma densities and are a mixture of L- and H-modes.

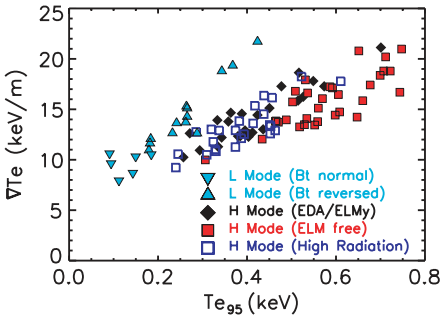

Fig. 27. The core temperature gradient is also seen to be tightly correlated with pedestal temperature, accounting for the increase in stored energy and confinement.

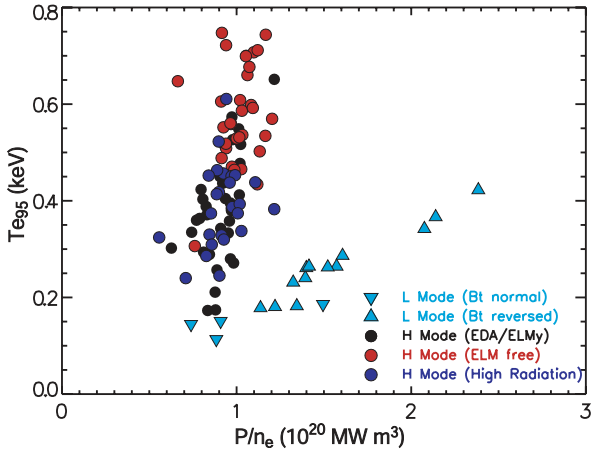

Fig. 28. Pedestal temperature plotted against power per particle. Following the results seen in Figs. 25, 26, and 27, the principal difference between core transport in L-mode and H-mode is the ease with which high edge temperatures are obtained in the latter regime.

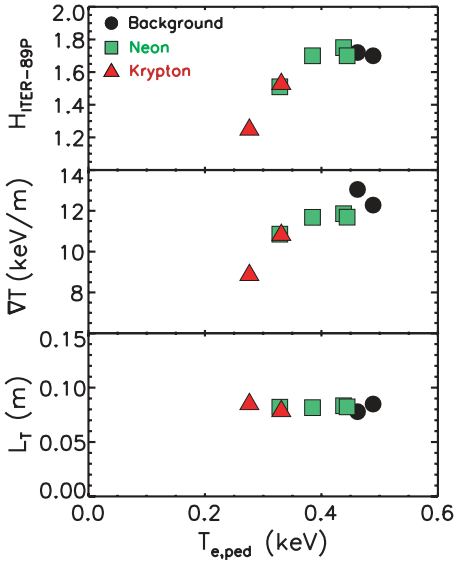

Fig. 29. A direct demonstration of the tight connection between edge and core temperatures was obtained in experiments in which radiating gases were puffed into developed H-modes. Radiation was peaked at $r/a \sim 0.8$ and resulted in a strong cooling of the pedestal. A corresponding decrease in core ∇T was observed, despite the fact that 90% of the radiated power was outside this radius. As in the global data set, the temperature scale length L_T remained constant.

temperatures with only modest heating. A direct demonstration of the tight coupling between edge and core temperatures was also obtained in experiments in which radiating gases were puffed into developed H-modes.[82] Radiation was peaked at $r/a \sim 0.8$ with 90% of the radiated power outside this radius, and thus there was almost no change to the power flux in the plasma core. The result was strong cooling of the pedestal and a corresponding decrease in core ∇T, as seen in Fig. 29.

Two important points are made by this set of plots. First, the difference in core energy confinement and thermal diffusivity between L- and H-mode can be understood to arise almost entirely from the difference in boundary conditions for the core temperature, rather than as intrinsic properties of core confinement in the

regimes. Of course, the presence of an edge transport barrier in H-mode makes it far easier to attain a high-temperature boundary. Second, the temperature scale length tends to be constant over a wide range of plasma conditions. This point is made clearly in Fig. 30, where the normalized gradient, defined as $R/L_T = R|\nabla T|/T$, is plotted against input power. This plot points out the inutility of thermal diffusivity in characterizing transport and suggests a different model for understanding these discharges—namely, the paradigm of marginal stability. In this model, transport is dominated by strong turbulence that is so efficient at transporting energy that the discharge remains near the stability boundary for the growth of the modes that underlie the turbulence. This picture can help explain Fig. 18, where L-mode confinement is maintained even as the conducted power is severely reduced. Conventional analysis would find χ dropping to extraordinarily low levels, especially in the outer portions of the plasma. However, from the perspective of marginal stability, it can be seen as the result of a temperature profile resilience given by the stability threshold and a boundary condition at the separatrix that is robust with respect to input power. Apparent anomalies in studies of heat pulse propagation are explainable in this context as well. It is well known that thermal diffusivity calculated from propagation of temperature perturbations typically exceeds the value calculated from power balance. In a set of C-Mod experiments, this effect grew stronger as input power was increased by almost an order of magnitude, with L_T changing only slightly. This is precisely the effect expected from a marginal stability model.

Theory predicts, in fact, that the microstability boundary for ion temperature gradient (ITG) turbulence, which should dominate in these types of discharges, corresponds to a threshold in R/L_T (Ref. 73). Marginal stability will be maintained, even at high power, as long as the turbulence is capable of conducting the input power effectively. For drift-wave–like turbulence, the maximum power that can be carried scales like $n_i T_i \rho_i^2$ and is well

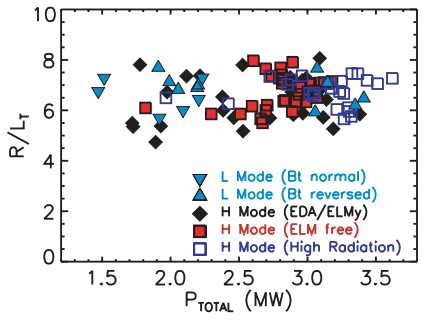

Fig. 30. Normalized temperature gradient R/L_T plotted against input power. The constancy of the gradient is consistent with marginal stability and the predictions of the critical gradient for ITG modes from theory.

above the power levels in the C-Mod (and most other) experiments. Careful modeling of C-Mod discharges using the gs2 code allowed quantitative comparisons between theory and experiment and helped to explain the inadequacy of early transport modeling,[80] as discussed in Sec. V.

While C-Mod pushed the range of parameter interpolation that was used to derive the models (particularly collisionality and magnetic shear), that does not seem to be the resolution of the problem. Bringing the predictions of these transport models into agreement with the experimentally measured temperature profiles would have required dropping the thermal diffusivity to unphysically low values. That is, the measured temperature gradient exceeded the predicted linear critical gradient by a wide margin. To investigate these matters, the gs2 code, which can solve the nonlinear gyrokinetic equations as an initial value problem in flux tube geometry with full electromagnetic and electron dynamic effects, was employed. This analysis showed that the discrepancy could be explained by a nonlinear upshift in the critical gradient due to the excitation and stabilizing influence of zonal flows.[83] Figure 31 shows the results of these calculations in a plot of conducted power versus normalized temperature gradient. Rough agreement with the experiments can be achieved only by a nonlinear calculation that includes all the relevant physics. These studies uncovered some interesting aspects of the nonlinear saturation of ITG turbulence and zonal flow damping. An important role for noncollisional damping of zonal flows was demonstrated along with the importance of maintaining nonadiabatic electron physics in these calculations.[80] The upshift could be artificially increased via unphysical assumptions of nonadiabatic electrons or by realistic assumptions of kinetic electrons in the higher collisionality of C-Mod H-modes.

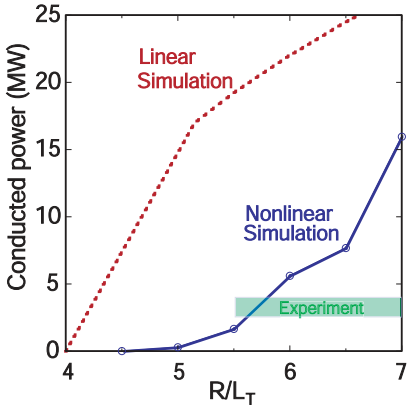

Fig. 31. Results of a detailed calculation of the critical gradient. The experimental heat flux and gradient are consistent with the nonlinear computation. The upshift in critical gradient in the calculation is due to stabilization of ITG turbulence by zonal flows. This result helps to explain the discrepancy seen in Fig. 24.

VII. IMPURITY TRANSPORT

As noted, the changes in confinement regimes are accompanied by changes in impurity transport. Using the laser blow-off technique,[84] nonrecycling, nonintrinsic impurities were injected into a variety of discharge types and their transport determined. Figure 32 compares the decay of injected impurities in these three discharge types.[34,70] For L-modes, the impurity confinement time τ_I was roughly equal to the energy confinement time τ_E and scaled in a similar fashion. In EDA or ELMy H-modes, τ_I rose to 2 to 3 $\times$ τ_E, while in ELM-free H-modes, τ_I was more than 10 $\times$ τ_E, often too long to measure accurately.[21] Figure 33 shows the rapid change in impurity particle transport for a discharge making a transition from ELM-free to EDA H-mode. The impurity diffusivity D_I in the core of EDA/ELMy discharges was comparable to the energy diffusivity and the main-ion particle diffusivity (in the range 0.4 to 0.8 m^2/s). However, the impurities were also subject to a strong inward pinch, perhaps 10 times larger than that of the main ions. Detailed analysis of impurity transport can be found in Refs. 3 and 70. These differences were reflected in the confinement of intrinsic impurities as well. The change in radiated power following an ELM-free to EDA transition was shown in Fig. 8 and was due to a change in molybdenum confinement.

A striking difference in impurity particle transport between regimes is also evident in the H-mode pedestals. An array of high-resolution soft X-ray detectors was used to measure the transport of impurities in the plasma edge.[45] Soft X-ray profiles were much narrower in ELM-free discharges than in those with EDA or ELMs, though with a width increasing with triangularity and q_{95} for both types. This observation suggests a deeper connection between particle transport and the ELM-free/EDA boundary that scales in the same way and with the same parameters. Transient analysis of the profiles following a transition found that the location of the X-ray pedestal could be attributed to a strong inward pinch located near the top of the pedestal. A strong pinch is to be expected from neoclassical theory because of the steep ion density gradient in this region. However, the cause of the difference in X-ray pedestal width was a change in impurity diffusivity, which rose from 0.01 m^2/s in ELM-free to about 0.04 in the EDA discharges studied. These values are essentially identical to the D_{eff} of the electrons, as shown in Fig. 11. The difference in electron density profile between the regimes was not as marked, however, perhaps reflecting the weaker collisional pinch expected for the main ions.

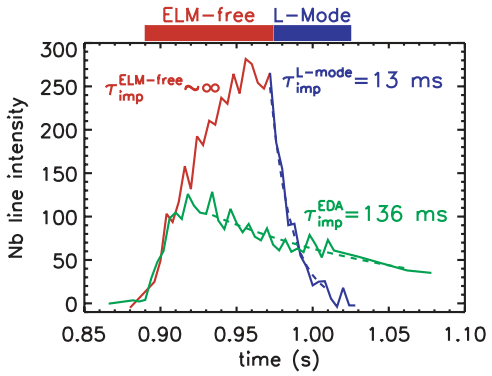

Fig. 32. Brightness of the niobium impurity lines following injection into two different discharges. After a brief influx phase, the impurity accumulated in an ELM-free discharge but not in the EDA discharge. The ELM-free H-mode was transient, and following its return to L-mode at 0.973 s, the rapid loss of the impurity was apparent.

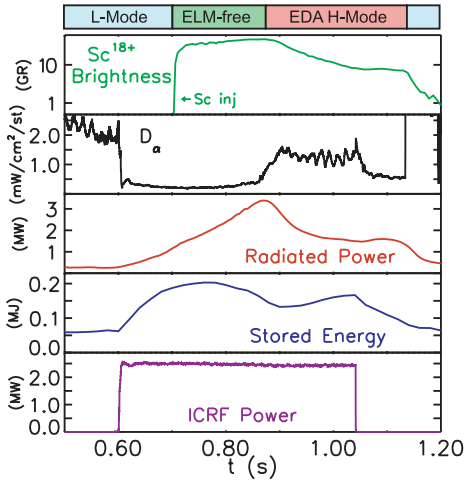

Fig. 33. The difference in impurity confinement between the H-mode regimes is clear in this discharge, where scandium was injected into a developed ELM-free plasma that later made a spontaneous transition to EDA at 0.86 s. The long impurity confinement time in the ELM-free phase contrasts with the decreased particle confinement in the EDA phase that followed.

VIII. DIMENSIONLESS IDENTITY, SIMILARITY, AND SCALING EXPERIMENTS

It may be possible to develop a better understanding and to improve capabilities for extrapolating that understanding to future devices by characterizing transport in terms of dimensionless parameters.[85] Two types of experiments have been carried out in this regard. First, in dimensionless "identity" experiments, discharges are run in devices of different sizes with all dimensionless quantities that are believed to be relevant matched. The dimensioned parameters will be quite different in each,

however. C-Mod can play an important role in such experiments since they require matching a small high-field device with a larger low-field one. These experiments are aimed at demonstrating the validity of the dimensionless scaling approach; that is, they attempt to determine if all the important parameters have been identified. In the second type of experiments, carried out in individual machines or between machines, all but one of the dimensionless parameters are matched, providing a relation between a dimensionless dependent variable and a single independent dimensionless parameter. These dimensionless "similarity" or "scaling" experiments may provide a more direct connection to the underlying plasma physics than scans of the engineering parameters. The dimensionless independent variables include geometric factors such as inverse aspect ratio ε, elongation κ, and triangularity δ and the plasma parameters q, the safety factor β, the normalized plasma pressure ν^*, the normalized collision frequency, and ρ^*, the inverse of the normalized plasma size. For transport studies, the commonly used dependent variables are $B\tau_E$, the confinement time normalized by the cyclotron frequency, and χ/χ_B, the thermal diffusivity normalized to Bohm diffusion.

Matching all of the dimensionless plasma parameters in devices of different sizes is equivalent to matching plasma shape, T_e/T_i, and the set of parameters nR^2, $BR^{5/4}$, $TR^{1/2}$, and $IR^{1/4}$. Then, if the plasma behavior depends only on these dimensionless variables, the input power required will match $PR^{3/4}$. Note that this requirement leads to a surface power density on the smaller of the machines in the comparison that is a factor of $(R_{large}/R_{small})^{11/4}$ higher than in the large experiment, limiting the range over which such experiments can be carried out. L-mode identity experiments performed between C-Mod and DIII-D are summarized in Table II, and sample profiles are shown in Fig. 34. The heating methods varied between the two machines, with C-Mod using ICRF and DIII-D heating with neutral beams. Power deposition was slightly more peaked for C-Mod, but the (normalized) integrated power, which is the quantity that enters into the transport calculations, is very similar. While the absolute value of the confinement time varied by almost a factor of 3, the properly normalized times agreed to within 10% (Ref. 86), comparable to experimental uncertainties. Local analysis showed an excellent match ($\pm$30%) in the normalized thermal diffusivity calculated in the range $r/a = 0.3$ to 0.9. A coordinated set of dimensionless identity experiments carried out by C-Mod, ASDEX-U, DIII-D, and JET showed similar agreement[87] for H-mode discharges. Table III summarizes the C-Mod–JET comparisons. The "correctness" of the dimensionless approach is such that even with a ratio of 55 in the power flux, a match in the normalized temperature profile was obtained. The near match in sawtooth frequency is also noteworthy. The success of these experiments suggests that at least for standard L- and H-mode plasmas, the dominant parameters that determine performance come from plasma physics. Atomic physics, which might be important in the plasma edge (and which can be

TABLE II

Parameters from Dimensionless Comparison of C-Mod and DIII-D L-Modes

	C-Mod	DIII-D
Engineering		
B (T)	5.22	1.61
a (m)	0.22	0.57
n_e (10^{20}/m^3)	1.80	0.26
P_{TOT} (MW)	3.2	1.9
τ_E (s)	0.027	0.079
Dimensionless		
R/a	3.07	3.06
$Ba^{5/4}$	0.79	0.79
na^2	0.85	0.82
β_{th} (%)	0.51	0.52
q_{95}	3.6	3.7
Bτ_E (T s)	0.141	0.127

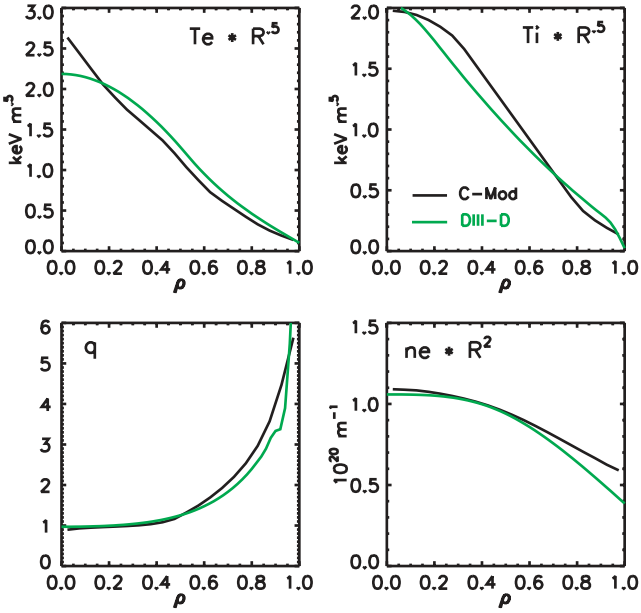

Fig. 34. Appropriately scaled plasma profiles for two discharges in a dimensionless identity comparison of C-Mod and DIII-D. Reasonable matches were obtained across the profiles. The largest difference was the somewhat more peaked power deposition obtained with ICRF heating on C-Mod compared to the NBI heating on DIII-D. Since it is the integrated power flux that enters the transport calculations, this difference is not believed to be important over most of the plasma.

TABLE III

Parameters from Dimensionless Identity Comparison of C-Mod and JET H-Modes

	C-Mod	JET
$10^4\rho^*$	2.7	2.8
$10^3\nu^*$	123	147
β_N	0.9	1.3
q_{95}	3.3	2.7
$B\tau_E$ (T s)	0.31	0.31
ELMs	None	None
$\frac{B_{C\text{-}Mod}}{B_{JET}} f_{Sawtooth}$	9	11

crucial in determining core confinement), was apparently not a significant factor in these cases. Particle and momentum sources from the neutral beams did not seem to have a dominant effect either. To further investigate a possible role for atomic physics, edge dimensionless identity experiments were carried out with DIII-D (Ref. 36). When the dimensionless parameters were matched at the top of the pedestal, the entire pedestal profile was seen to match (Fig. 35). Since the dimensionless parameters associated with atomic physics were not matched for these experiments, the results provide a prima facie case that plasma physics rather than neutral penetration or radiation determines the pedestal structure.

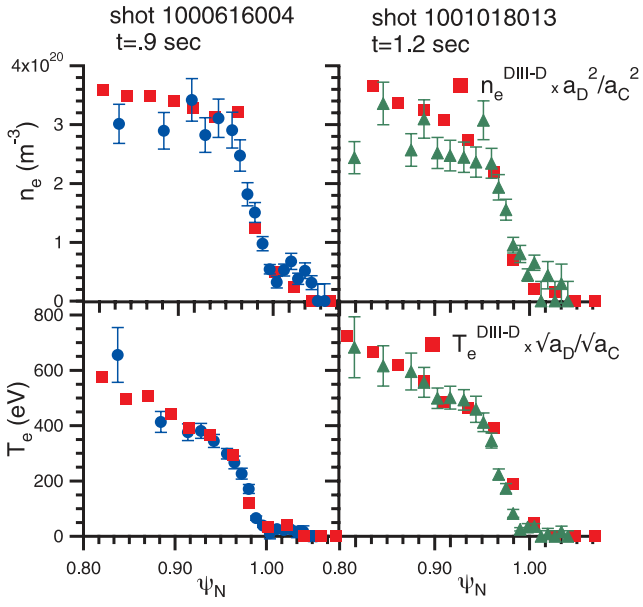

Fig. 35. A pair of dimensionless pedestal comparisons, from C-Mod and DIII-D, shows that the entire profile could be matched, suggesting a primary role for plasma physics in determining the edge profiles. C-Mod data are shown as circles and diamonds; DIII-D profiles are plotted as squares.

A series of experiments was carried out to measure the scaling of transport with ρ^* and ν^* in C-Mod.[77,78] To perform the ρ^* scans, the magnetic field was scanned from 2.6 to 5.3 T. Holding β and ν^* constant requires plasma density to be scaled as $B^{4/3}$ and temperature as $B^{2/3}$. This takes substantially more power for the higher-field discharge and limits the range of ρ^* possible in any single machine. Table IV gives parameters for a particular matched pair of H-mode discharges. Combining the results from a number of experiments gave $B\tau_E \propto \rho^{*-3.4\pm1.0}$, that is, a scaling somewhat stronger than gyro-Bohm. Scans in L-mode plasmas gave the Bohm-like scaling $B\tau_E \propto \rho^{*-1.8\pm0.6}$. In both cases the error bars are relatively large because of the narrow range in ρ^*. It is relatively easy to scan over a wide range in ν^* while holding the dimensionless quantities fixed. For L-mode, the field and current were varied by a factor of 2, from 2.6 to 5.3 T, while the plasma density was kept constant. By applying higher powers to the high-field cases, the temperature was raised to four times that of the corresponding low-field cases, keeping β and ρ^* unchanged. The low-field discharge then has a collisionality 16 times that of the high-field plasma. Table V compares some representative quantities for a pair of matched H-mode discharges, with a somewhat smaller range in ν^*. The results from a broader data set can be seen in Fig. 36, where the dimensionless energy confinement time is seen to degrade at higher ν^* as $B\tau_E \sim \nu^{*-1.0\pm0.2}$. Similar experiments carried out in L-mode plasmas yielded a weaker degradation with collisionality, $B\tau_E \sim \nu^{*-0.4\pm0.1}$.

TABLE IV

Parameters for Dimensionless ρ^* Scaling Experiment in C-Mod H-Modes

	Shot	
	960118016	960130020
Engineering		
B_T (T)	2.5	5.4
I_P (MA)	0.5	1.1
n_e (10^{20}/m^3)	1.38	2.90
P_{RF} (MW)	0.92	2.01
Dimensionless		
β_T (%)	1.10	1.03
q_{95}	3.26	3.23
ν^*	0.54	0.40
T_i/T_e	0.87	1.01
P_{RAD}/P_{TOT}	0.18	0.13
$1000\rho^*$	6.24	4.21
$B\tau_E$ (T s)	0.06	0.22

TABLE V

Parameters for Dimensionless ν^* Scaling Experiment on C-Mod

	Shot	
	960118030	960130020
Engineering		
B_T (T)	2.6	5.3
I_P (MA)	0.6	1.1
n_e (10^{20}/m^3)	2.25	2.6
P_{RF} (MW)	0.93	1.99
Dimensionless		
β_T (%)	1.28	1.14
q_{95}	3.24	3.19
$1000\rho^*$	4.90	4.68
T_i/T_e	0.92	1.0
P_{RAD}/P_{TOT}	0.11	0.08
ν^*	1.10	0.23
Bτ_E (T s)	0.06	0.30

These results were at least superficially in agreement with theoretical models. Higher collisionalities have been predicted to damp zonal flows and thus increase the level of saturated turbulence.[88]

IX. SUMMARY

Confinement in the low-density ($n_e q < 4\times10^{20}$/m^3), linear ohmic (Alcator) regime matched previously derived scaling laws. At higher densities, the density dependence saturated and confinement was equivalent to L-mode. For this regime and rf-heated L-modes, confinement agreed well with the ITER89 scaling. H-mode data from C-Mod averaged well above the ITER93 and ITER94 H-mode laws, pointing out the risks in extrapolating these empirical fits. The difficulty likely arose because of the limited range and correlation between independent variables in the original database. Addition of C-Mod data improved the conditioning of the H-mode database; unconstrained fits performed after the inclusion of C-Mod data obeyed the Connor-Taylor relations, which was not the case earlier. Unlike other experiments, C-Mod H-modes do not have large type I ELMs. Instead, the pedestal gradients are regulated by small ELMs or a continuous QC mode. The latter regime has been dubbed EDA for enhanced D_α and is quasi-steady, with good energy confinement and no impurity accumulation. EDA H-modes are prevalent at higher q, higher triangularity, and higher collisionality and with lower ion mass. These dependences along with theoretical studies suggest that the QC mode is a form of resistive ballooning. With higher pedestal pressure gradients and lower collisionality, small (likely type II) ELMs emerge and take over pedestal regulation from the QC mode. C-Mod temperature profiles were self-similar, with the gradient proportional to the temperature. This observation demonstrated the first quantitative link between edge temperatures, core temperature gradients, and core confinement, consistent with theoretical predictions of marginal stability to ITG turbulence near a critical gradient length. L- and H-modes thus have similar intrinsic transport properties but differ because the edge transport barrier allows the production of a high-temperature edge boundary condition. C-Mod H-mode temperature profiles could not be predicted, initially, by existing theory-based models. Nonlinear gyrokinetic simulations showed that the change in electron dynamics induced at the higher collisionality led to an increase in the upshift of the critical temperature gradient. Local transport studies demonstrated connections between transport channels, with energy, particle, and momentum transport varying across regimes in similar ways. The ability to measure rotation dynamics in torque-free discharges led to the unexpected observation of strong, self-generated toroidal flows in C-Mod. Dimensionless identity experiments, carried out in collaboration with DIII-D, ASDEX-U, and JET confirmed this approach over the widest available range in machine sizes. Nondimensional scaling of edge parameters showed that the pedestals scaled with the dimensionless variables of plasma physics, not atomics physics. Dimensionless scaling experiments showed a strong improvement in confinement with the normalized gyro size ($1/\rho^*$). Confinement was found to be Bohm-like in L-mode and gyro-Bohm–like in H-mode. These experiments also showed a strong degradation in confinement with collisionality, in agreement with expectations of linear zonal flow damping.

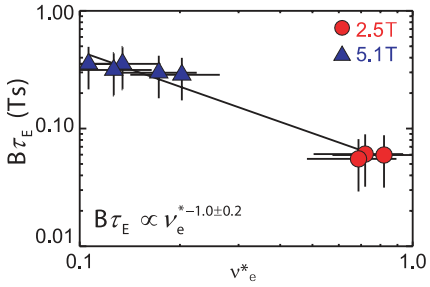

Fig. 36. An example of dimensionless scaling, in which the normalized confinement time is plotted against collisionality with all other dimensionless parameters (β, ρ^*, ε, δ, κ, etc.) held constant. The decrease in confinement at higher collisionality is consistent with predictions from theories of collisional damping of zonal flows.

ACKNOWLEDGMENT

Alcator C-Mod is supported by U.S. Department of Energy contract DE-FC02-99ER54512.

REFERENCES

1. P. T. BONOLI et al., "Wave-Particle Studies in the Ion Cyclotron and Lower Hybrid Ranges of Frequencies in Alcator C-Mod," *Fusion Sci. Technol.*, **51**, 401 (2007).

2. N. P. BASSE et al., "Diagnostic Systems on Alcator C-Mod," *Fusion Sci. Technol.*, **51**, 476 (2007).

3. J. E. RICE et al., "Impurity Transport in Alcator C-Mod Plasmas," *Fusion Sci. Technol.*, **51**, 357 (2007).

4. J. E. RICE et al., "Spontaneous Toroidal Rotation in Alcator C-Mod Plasmas with No Momentum Input," *Fusion Sci. Technol.*, **51**, 288 (2007).

5. J. W. HUGHES et al., "H-Mode Pedestal and L-H Transition Studies on Alcator C-Mod," *Fusion Sci. Technol.*, **51**, 317 (2007).

6. C. L. FIORE et al., "Internal Transport Barriers in Alcator C-Mod," *Fusion Sci. Technol.*, **51**, 303 (2007).

7. R. PARKER, M. GREENWALD, S. LUCKHARDT, E. MARMAR, M. PORKOLAB, and S. WOLFE, *Nucl. Fusion*, **25**, 1127 (1985).

8. M. GREENWALD et al., *Phys. Plasmas*, **2**, 2308 (1995).

9. C. FIORE et al., *Phys. Plasmas*, **11**, 2480 (2004).

10. D. GARNIER et al., "Formation and Evolution of Internal Transport Barriers in Alcator C-Mod," *Proc. IAEA 16th Int. Conf. Plasma Physics and Controlled Nuclear Fusion Research*, Montreal, Canada, October 7–11, 1996, International Atomic Energy Agency, Vol. 1, p. 907 (1997).

11. M. GREENWALD et al., *Phys. Rev. Lett.*, **53**, 352 (1984).

12. S. WOLFE et al., *Phys. Plasmas*, **12**, 56110-1 (2005).

13. R. GOLDSTON, *Plasma Phys. Control. Fusion*, **26**, 87 (1984).

14. R. HAWRYLUK, in *Physics of Plasmas Close to Thermonuclear Conditions*, Varenna, Italy, August 27–September 8, 1979, Pergamon Press, Oxford, England, Vol. 1, p. 19 (1980).

15. A. GONDHALEKAR et al., "Study of the Energy Balance in Alcator," *Proc. IAEA Seventh Int. Conf. Plasma Physics and Controlled Nuclear Fusion Research*, Innsbruck, Austria, August 23–30, 1978, International Atomic Energy Agency, Vol. 1, p. 199 (1979).

16. M. GREENWALD et al., "Studies of the Regime of Improved Particle and Energy Confinement Following Pellet Injection into Alcator C," *Proc. IAEA 11th Int. Conf. Plasma Physics and Controlled Nuclear Fusion Research*, Kyoto, Vol. I, p. 139 (1987).

17. P. YUSHMANOV et al., *Nucl. Fusion*, **24**, 1999 (1990).

18. J. FREIDBERG et al., "Alcator C-Mod Proposal," MIT-PFC RR-85-18, DOE/ET-51013-158, Massachusetts Institute of Technology (1985).

19. Y. TAKASE et al., *Plasma Phys. Control. Fusion*, **38**, 2215 (1996).

20. F. RYTER et al., *Plasma Phys. Control. Fusion*, **38**, 1279 (1996).

21. M. GREENWALD et al., *Nucl. Fusion*, **37**, 793 (1997).

22. J. SNIPES et al., *Phys. Plasmas*, **3**, 1992 (1996).

23. J. SNIPES et al., *Nucl. Fusion*, **34**, 1039 (1994).

24. A. HUBBARD et al., *Plasma Phys. Control. Fusion*, **40**, 689 (1998).

25. A. HUBBARD et al., *Plasma Phys. Control. Fusion*, **46**, A95 (2004).

26. P. GUZDAR et al., *Phys. Plasmas*, **11**, 1109 (2004).

27. B. LaBOMBARD et al., *Nucl. Fusion*, **44**, 1047 (2004).

28. M. GREENWALD et al., *Nucl. Fusion*, **28**, 2199 (1988).

29. J. RICE et al., *Nucl. Fusion*, **38**, 75 (1998).

30. H. ZOHM, *Plasma Phys. Control. Fusion*, **38**, 1213 (1996).

31. J. SNIPES et al., *Plasma Phys. Control. Fusion*, **38**, 1127 (1996).

32. J. SNIPES et al., *Plasma Phys. Control. Fusion*, **40**, 765 (1998).

33. P. STEK, "Reflectometry Measurements on Alcator C-Mod," PhD Thesis, Massachusetts Institute of Technology (1997).

34. M. GREENWALD et al., *Phys. Plasmas*, **6**, 1943 (1999).

35. M. BURES et al., *Nucl. Fusion*, **32**, 539 (1992).

36. D. A. MOSSESSIAN et al., *Phys. Plasmas*, **10**, 689 (2003).

37. K. KAMIYA et al., *Plasma Phys. Control. Fusion*, **46**, 1745 (2004).

38. K. McCORMICK et al., *J. Nucl. Mater.*, **337–339**, 520 (2005).

39. S. MIRNOV et al., *Nucl. Fusion*, **39**, 2251 (1999).

40. M. GREENWALD et al., *Plasma Phys. Control. Fusion*, **42**, A263 (2000).

41. Y. KAMADA et al., *Plasma Phys. Control. Fusion*, **42**, A247 (2000).

42. D. MOSSESSIAN et al., *Plasma Phys. Control. Fusion*, **44**, 423 (2002).

43. D. MOSSESSIAN et al., *Phys. Plasmas*, **10**, 1720 (2003).

44. H. R. WILSON, P. SNYDER, et al., *Phys. Plasmas*, **9**, 1277 (2002).

45. T. SUNN PEDERSEN et al., *Nucl. Fusion*, **40**, 1795 (2000).

46. J. SNIPES et al., *Plasma Phys. Control. Fusion*, **43**, L23 (2001).

47. N. BASSE et al., *Phys. Plasmas*, **12**, 52512-1 (2005).

48. A. MAZURENKO et al., *Phys. Rev. Lett.*, **89**, 225004-1 (2002).

49. A. HUBBARD et al., *Phys. Plasmas*, **8**, 2033 (2001).

50. R. SLUSHER et al., *Phys. Rev. Lett.*, **53**, 667 (1984).

51. G. TYNAN, *Phys. Plasmas*, **1**, 3301 (1994).

52. R. MOYER et al., *J. Nucl. Mater.*, **266–269**, 1145 (1999).

53. B. ROGERS and J. DRAKE, *Phys. Plasmas*, **6**, 2797 (1999).

54. L. GARCIA, B. CARRERAS, and V. LYNCH, *Phys. Plasmas*, **6**, 107 (1999).

55. B. ROGERS, J. DRAKE, and A. ZEILER, *Phys. Rev. Lett.*, **81**, 4396 (1998).

56. X. XU, *Phys. Plasmas*, **7**, 1951 (2000).

57. W. NEVINS et al., "Simulations of Boundary Turbulence in Tokamak Experiments," *Proc. 19th Conf. Fusion Energy*, Lyon, France, October 14–19, 2002, International Atomic Energy Agency (2002); available on the Internet at http://www.pub.iaea.org/MTCD/publications/PDF/csp_019c/pdf/thp3_07.pdf.

58. W. DORLAND, F. JENKO, M. KOTSCHENREUTHER, and B. N. ROGERS, *Phys. Rev. Lett.*, **85**, 5579 (2000).

59. ITER H MODE DATABASE WORKING GROUP, *Nucl. Fusion*, **34**, 131 (1994).

60. ITER EXPERT GROUPS ON CONFINEMENT, TRANSPORT, CONFINEMENT MODELING AND DATABASES, *Nucl. Fusion*, **39**, 2175 (1999).

61. J. G. CORDEY et al., *Plasma Phys. Control. Fusion*, **39**, B115 (1997).

62. ASDEX TEAM, *Nucl. Fusion*, **29**, 1959 (1989).

63. B. LaBOMBARD, *J. Nucl. Mater.*, **241–243**, 149 (1997).

64. B. LaBOMBARD, *Phys. Plasmas*, **12**, 056111 (2005).

65. J. SNIPES et al., *Proc. 24th EPS Conf. Controlled Fusion and Plasma Physics*, Berchtesgaden, Germany, June 9–13, 1997, European Physical Society, Vol. 21A, Part II, p. 565 (1997).

66. M. BRAMBILLA, *Plasma Phys. Control. Fusion*, **41**, 1 (1999).

67. G. HAMMETT, "Fast Ion Studies of Ion Cyclotron Heating in the PLT Tokamak," PhD Thesis, Princeton University (1986).

68. L. LAO et al., *Nucl. Fusion*, **25**, 1611 (1985).

69. T. LUKE, "Measurement of Particle Transport Coefficients on Alcator C-Mod," PhD Thesis, Massachusetts Institute of Technology (1994).

70. J. RICE et al., *Phys. Plasmas*, **4**, 1605 (1997).

71. W. D. LEE et al., *Phys. Rev. Lett.*, **91**, 205003/1 (2003).

72. S. WOLFE et al., *Nucl. Fusion*, **26**, 329 (1986).

73. M. KOTSCHENREUTHER, W. DORLAND, M. BEER, and G. HAMMETT, *Phys. Plasmas*, **2**, 2381 (1995).

74. R. WALTZ et al., *Phys. Plasmas*, **4**, 2483 (1997).

75. G. BATEMAN et al., *Phys. Plasmas*, **5**, 1793 (1998).

76. D. BOUCHER et al., *Nucl. Fusion*, **40**, 1955 (2000).

77. J. SCHACHTER, "Local Transport Analysis for the Alcator C-Mod Tokamak," PhD Thesis, Massachusetts Institute of Technology (1997).

78. M. GREENWALD et al., *Plasma Phys. Control. Fusion*, **40**, 789 (1998).

79. A. PANKIN et al., *Phys. Plasmas*, **8**, 4403 (2001).

80. D. MIKKELSEN et al., "Nonlinear Simulations of Drift-Wave Turbulence in Alcator C-Mod," *Proc. 19th Conf. Fusion Energy*, Lyon, France, October 14–19, 2002, International Atomic Energy Agency (2002).

81. F. RYTER et al., *Plasma Phys. Control. Fusion*, **40**, 725 (1998).

82. A. HUBBARD et al., *Proc. 26th EPS Conf. Controlled Fusion and Plasma Physics*, Maastricht, The Netherlands, June 14–18, 1999, European Physical Society, Vol. 23J, p. 13 (1999).

83. A. DIMITS et al., *Phys. Plasmas*, **7**, 969 (2000).

84. E. MARMAR, J. CECCHI, and S. COHEN, *Rev. Sci. Instrum.*, **46**, 1149 (1975).

85. J. CONNOR and J. TAYLOR, *Nucl. Fusion*, **17**, 1047 (1977).

86. T. LUCE et al., *Nucl. Fusion*, **42**, 1193 (2002).

87. J. CHRISTIANSEN et al., "Experimental Tests of Confinement Scale Invariance on JET, DIII-D, AUG, and C-Mod," *Proc. IAEA 17th Int. Conf. Plasma Physics and Controlled Nuclear Fusion Research*, Yokohama, Japan, October 19–24, 1998, Vol. 2, p. 765 (2000).

88. M. ROSENBLUTH and F. HINTON, *Phys. Rev. Lett.*, **80**, 724 (1998).